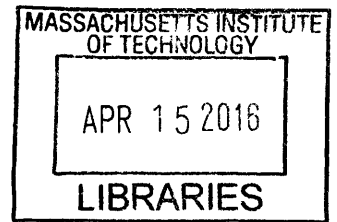


**Wide-field Magnetic Field Imaging with Nitrogen
Vacancy Centers in Nanodiamonds at High
Frame-rates**

by
Christopher Foy



Submitted to the Department of Electrical Engineering and Computer
Science

in partial fulfillment of the requirements for the degree of

Master of Science in Electrical Engineering and Computer Science

at the

MASSACHUSETTS INSTITUTE OF TECHNOLOGY

February 2016

© Massachusetts Institute of Technology 2016. All rights reserved.

Author .. **Signature redacted**
Department of Electrical Engineering and Computer Science
January 29, 2016

Certified by **Signature redacted**

Dirk Englund
Assistant Professor
Thesis Supervisor

Accepted by **Signature redacted**
 Leslie A. Kolodziejski
Chairman, Department Committee on Graduate Theses

Wide-field Magnetic Field Imaging with Nitrogen Vacancy Centers in Nanodiamonds at High Frame-rates

by

Christopher Foy

Submitted to the Department of Electrical Engineering and Computer Science
on January 29, 2016, in partial fulfillment of the
requirements for the degree of
Master of Science in Electrical Engineering and Computer Science

Abstract

The nitrogen vacancy center (NV) is a promising single spin system in diamond with optical polarization, readout and optically detected magnetic resonances (ODMR). The NV has been shown to be a sensitive magnetometer at room temperature. In particular, owing to their small size, NV centers in nanocrystals (nanodiamonds) offer magnetic field imaging with high spatial resolution. Competitive magnetic field imaging methods such as magnetic force microscopy (MFM) or superconducting quantum interference devices (SQUID) either image serially, and are thus slow, or are limited in their use for biological systems. Nanodiamonds in contrast have the advantage that they can be attached to biological tissues *in vivo* and can be imaged in parallel at high speeds. Unfortunately, nanodiamonds tend to aggregate due to Coulomb interactions of their surface species. This aggregation results in an inhomogeneous broadening of the NV's ODMR with applied magnetic field. This broadening makes imaging magnetic fields non-trivial. In this work, we present a model to understand aggregated nanodiamonds. Despite NVs with defined crystallographic orientations demonstrating vectorial resolution of magnetic fields, this model predicts that aggregated nanodiamonds should be treated as absolute magnetometers. Further, a sparse sampling protocol is implemented that enables time resolved magnetometry and is used to image the magnetic field of a current carrying wire at greater than 33 Hz speeds with magnetic field sensitivities better than $2 \mu\text{T}/\sqrt{\text{Hz}}$ over a $10 \mu\text{m} \times 10 \mu\text{m}$ field of view.

Thesis Supervisor: Dirk Englund
Title: Assistant Professor

Acknowledgments

I would like to acknowledge Carl Sagan whose calm voice pushed a young mind to explore science. A large thanks is given to my high school physics teacher Dr. Houston who encouraged me to pursue physics. He was an under-appreciated jewel and his passion for the sciences was instilled in me. Further, I would like to thank Kurt Broderick and James Dayley for teaching me fabrication skills. They were also very kind to act as sounding boards to bounce ideas off of. These technicians were always willing to offer feedback and give advice and I am very grateful. I am lucky to know them. I would also like to thank David L Lewis at the Cypress Machine Shop. His help in learning machining was invaluable in the completion of this work.

This thesis could not have been assembled without help from Matt Trusheim. His input was essential for developing many of the ideas that make up this work. My colleague Adam McCaughan deserves acknowledgment as his help was very appreciated in learning the skills to perform wire bonding. Sinan Karaveli is also a person whom I would like to offer thanks. His ability to use every piece of equipment in the lab was very helpful and he has taught me much. While we are forced to work together because we share an optical table, I am glad to consider you a friend. Of course my fellow colleagues, whom are too many to be stated here, deserve my sincerest gratitude.

I would also like to thank my friends in the Ashdown student government who I work with daily to improve the lives of the residents of the dorm. Their emotional support is appreciated. I would also like to thank Siyuan Zhu for the thankless, and perhaps unknown, job of frequently texting me during the writing of this thesis to confirm that I had not yet shed my mortal coil.

My friends that I made at Georgia Tech also deserve an acknowledgment. These fellow students, and our shared memories, will always be remembered fondly. Here is a thanks to all these friends who live on distant shores. May time never shred our bonds.

I would also like to thank my family. They supported me when I was too young to support myself and for better or worse, shaped me into who I am today. To my

brothers whom I frequently fought with in my youth, I would also like to thank. Of course a special thanks should be given to my mother and father.

Finally I would like to acknowledge my advisor, Dirk Englund. His help was invaluable. I am sure his advice will be appreciated in the coming years as I strive to complete my PhD.

Contents

1	Introduction	17
2	Theory and Overview	21
2.1	General diamond properties	21
2.2	Overview of the Nitrogen Vacancy Center	22
2.3	NV Physics	24
2.4	NV Interactions with Magnetic Fields	25
2.5	ODMR Measurements for an NV	27
2.6	Magnetic Sensitivity for DC Magnetic Fields	29
2.7	Introduction to the Experimental Setup	32
2.8	NVs within Nanodiamonds	33
3	Modeling	36
3.1	Simulations of NVs with in a Diamond Lattice	36
3.2	Nanodiamond Properties	40
3.3	NV Polycrystalline Modeling	43
3.4	Mapping NV Fluorescence to Magnetic Field	49
4	Fabrication	54
4.1	Liftoff	54
4.1.1	Photolithography	54
4.2	Electron Beam Physical Vapor Deposition	60
4.3	Electroplating	65

5	Overview of the Experiment and Results	71
5.1	Overview of Experimental Setup	71
5.2	Overview of the Experiment	75
5.3	Experimental Results: Magnetic Imaging	77
6	Conclusion and Outlook	81

List of Figures

1-1	Neural Activity captured by an fMRI machine. Taken from Wikipedia [61].	18
2-1	Illustration of an NV center (a) A model of an FCC diamond. Picture taken from Wikipedia [57]. (b) This illustration shows that an NV is formed when a nitrogen atom (N) replaces a carbon atom (C) and is adjacent to a missing carbon atom. This missing carbon atom is called a vacancy (V). This arrangement is called a nitrogen vacancy center.	22
2-2	The spectrum of the two types of fluorescent NVs. The blue curve is NV^0 and the red is NV^- . NV^- is red shifted compared to the NV^0 allowing for these charge states to be spectrally discriminated. The initial peak is known as the ZPL and it is marked for each spectrum.	23
2-3	Energy level diagram of an NV. The leftmost set of levels (3A and 3E) are the electronic orbital states and are triplet states. The 3A has a splitting of 2.87 GHz between its $m_s = 0\rangle$ and $m_s = \pm 1\rangle$ spin states. These states can be separated by applying a magnetic field that has a component aligned with the NV's axis. The excited $m_s = \pm 1\rangle$ spin states exhibit an intersystem crossing to a metastable 1A level which has a relaxation back to the $m_s = 0\rangle$ ground state through the emission of an infrared photon.	24

2-4	Position of an NV's resonant frequency as a function of B_{NV} . The red curve represents an ideal NV system and it showcases a zero field splitting located at 2.87 GHz. The slope is equal to 0.028 MHz/ μ T. The black curve represents an NV within a strained diamond. There is a splitting even at zero magnetic field which is equal to $2E$ [42].	26
2-5	NV ODMR spectra (a) ODMR spectrum of a single NV at different magnetic fields. These ODMR curves are a combination of the NV's Hamiltonian (where the resonances are positioned), spin selective shelving state of the NV (the mechanism for the drop in intensity) and a Lorentzian which is centered about each resonance. (b) An ODMR of an NV ensemble comprised of all four orientations of the NV within a bulk diamond lattice, with one pair degenerate at $D = 2.87$ GHz. Since the NVs are within the diffraction limit of one another, the measured ODMR curve will be the sum of each orientation's ODMR.	28
2-6	Display of sensitivity parameters. FWHM and Contrast are shown for an NV's ODMR spectra.	31
2-7	An image of a schematic diagram of a spin microscope.	32
2-8	CWESR pulse sequence for an ODMR measurement.	33
2-9	Illustration of an NV ensemble within a nanodiamond. Each arrow represents an NV center. The nanodiamonds can be as small as a few nm in size and can contain between one to hundreds of NVs.	34
2-10	In vitro ODMR measurements of NVs within nanodiamonds attached to neuronal membranes The top left image shows a bright-field image of a neuron. The top right image shows a fluorescence image of a neuron stained with NV centers. The two bottom images show the ODMR curves from nanodiamonds attached to the neuronal membrane. In vitro ODMR measurements on these attached NVs demonstrate biological compatibility.	35

3-1	Fitting workflow to extract sensing information from an NV's ODMR curve.	36
3-2	Fitting Lorentzians to the NV ODMR's curve. The ODMR curve is the black curve and the Lorentzians are the blue curves. All four NV orientations are degenerate.	37
3-3	Schematic of the orthogonal vectors, $\hat{\mathbf{v}}_1$ and $\hat{\mathbf{v}}_2$, to the NV axis . . .	38
3-4	Curve fits of NV ODMR spectra (a) A large magnetic field was applied to separate all four NV orientations. The ODMR curve was fitted to determine B_x , B_y , B_z and the lattice orientation. (b) The red curve was generated when 20 mA DC current was applied through the solenoid oriented above the sample. The parameters shown in table 3.1 were determined from Fig.3-4a and then recycled leaving only the electromagnet's conversion efficiency at the sample plane, ζ , as the only remaining fit parameter. This parameter was determined from the blue fit. A value of -26 $\mu\text{T}/\text{mA}$ was determined as the overall magnetic field conversion parameter.	41
3-5	Measured ODMR spectra of NVs within nanodiamond (a) Fluorescence image of deposited commercially available Adámas nanodiamonds. The ODMR spectra of the selected nanodiamond with increasing magnetic field is shown in figures b-d. (b) ODMR of an ensemble of NVs within the nanodiamond at low magnetic field.(c) ODMR of an ensemble of NVs within a nanodiamond at 1125 μT applied field. (d) ODMR curves of an ensemble of NVs within a nanodiamond measured at increasing magnetic field. Note the drop in contrast and the broadening of the ODMR curve.	42
3-6	Contour plot of the contrast as a function of frequency and magnetic field.	43

3-7 **Illustration of two different NV models** The top image shows NVs within defined crystallographic orientations such as those found in bulk diamond systems. The bottom image represents NVs found in aggregated polycrystalline diamond. The NVs are modeled to be spherically symmetrical around an origin. 44

3-8 ODMR curve taken at low magnetic fields to determine static parameters such as strain, linewidth and contrast. 45

3-9 Fitted ODMR curves for an ensemble of NVs within a nanodiamond as a function of magnetic field. These result confirm the validity of the polycrystalline model. 46

3-10 A histogram of sensitivity of these aggregated nanodiamond systems. 46

3-11 **Response curves of different NV systems** (a) Contrast recorded at 2.87 GHz as a function of magnetic field. This is called a response curve. (b) Simulated response curves of different NV systems. It is shown that a single NV has a very different response to magnetic field compared to aggregated ensembles. Error bars on this plot refer to the standard deviation of normalized fluorescence resulting from varying the NV's orientation. The solid curves are the averaged values over all orientations. 47

3-12 Simulated calculation of the magnetic field for different NV systems assuming a mapping based on the response curve of a single NV with increasing B_{NV} . Error bars on this plot refer to the standard deviation of normalized fluorescence resulting from varying the NV's orientation. The solid curves are the averaged values over all orientations. 49

3-13	Analysis of first-order truncation mapping (a) First-order truncation mapping using tangent lines located at $D \pm w/2$. (b) Simulated accuracy of the first-order truncation mapping. This mapping is not ideal for NV ensembles, giving a large error when calculating the magnetic field. Errors greater than $\simeq 300 \mu\text{T}$ across many applied magnetic field magnitudes are observed. Error bars on this plot refer to the standard deviation of normalized fluorescence resulting from varying the NV's orientation. The solid curves are the averaged values over all orientations.	50
3-14	Nanodiamond calibration procedure (a) Mapping a response curve by sampling the contrast at one frequency point with a known magnetic field value. In this instance the contrast is recorded with an applied field of $300 \mu\text{T}$. (b) The response curve was mapped and fitted to a second-order polynomial. This resulting polynomial is shown above.	51
3-15	Accuracy of calibration procedure (a) This calibration method of fitting an NV ensemble's response curve is used to sense a changing magnetic field. (b) The accuracy of fitting an NV ensemble's response curve to sense magnetic field is shown as a function of $\Delta\tau$. Increasing the measurement time reduces the error before the accuracy settles to some systemic error.	52
4-1	This figure gives an overview of Photolithography, where resist is exposed to UV light through a masking layer. Two types of resist are illustrated. On the left is a positive resist and it behaves as described earlier. However, on the right is a negative resist that behaves oppositely. Regions that are exposed harden, unlike a positive resist. In this way, designs on the masking layer can be imprinted onto the resist.	56

4-2 A schematic illustrating how a spin coater operates. As the substrate is rotated the deposited material flattens and becomes planar. By varying this speed the resist can be tuned to a desired thickness. This image was taken from Wikipedia [3]. 57

4-3 **Baking glass slides** (a) A sample is placed in an aluminum cup and weighed down to create a uniform thermal contact between the substrates. (b) Glass slides have very little weight and when placed on an aluminum foil or hotplate, do not have good thermal contact. The poor contact with the aluminum foil means their will not be a uniform bake and some regions of the substrate will not cross link. 58

4-4 **Bright-field images of developed samples** (a) An image of a well-developed sample. A clear contrast between the regions can be observed. (b) An image of an insufficiently developed sample. Large discolorations are a result of thickness variations across the sample. 59

4-5 EBPVD schematic. Electrons are emitted by a tungsten filament and guided by a perpendicular magnetic field. These electrons impact and sublime the metal in the crucible. This sublimated metal is deposited onto the sample. This image was taken from Wikipedia [59]. 60

4-6 Possible side wall profiles from photolithography. The top image is a bad side wall profile. Deposited metal will form metal bridges which can ruin the liftoff. The second profile is acceptable and the third profile is ideal for a successful liftoff. 61

4-7	EBPVD procedure (a) Image of the EBPVD Tray. Avoid making excessive contact between the mounting tape and the glass coverslips. (b) EBPVD pressure sensor and controller. Program deposited material sequentially to correctly calibrate the EBPVD sensor. (c) EBPVD tray post deposition. The entire tray is covered in deposited material. (d) White light image of a completed and wirebonded sample. The gold wire is a wire bond that is bonded off chip. High frequency alternating (AC) current is transmitted through the thick outer wire which generates microwave fields at the location of the NVs. A similar structure will carry DC current.	62
4-8	Two ODMR curves showing the effects of an increase in temperature of 6 K. Error bars are omitted on the second ODMR curve for clarity.	64
4-9	Spatial Mapping of the increase in temperature (a) D parameter mapping at 0 mA applied DC current through the fabricated structure. (b) D parameter mapping at 20 mA applied DC current through the fabricated structure.	64
4-10	A diagram giving an overview of electroplating. A current is run through a metal sample that is placed into a solution of metal ions. The metal ions attach to the surface through Coulomb interactions. This creates a deposition layer. The rate of deposition and the location can be controlled to create structures. This image was taken from Wikipedia [60].	66
4-11	The electroplating current controller.	66
4-12	Profilometer measurements on electroplated sample (a) Sample step profile when structures are plated too quickly. A high surface roughness is observed. (b) Sample step profile when structures are plated slower. A reduction in surface roughness is observed. The height differential between points h_1 and h_2 is $\simeq 2 \mu\text{m}$	68
4-13	Image of the sample holder when a sample is clipped in.	68

4-14	Sample after electroplating (a) Picture of a finished electroplated sample on the profilometer stage. (b) A bright-field image of a finished electroplated sample. The black particles that cover the structure are nanodiamonds that were placed onto the surface afterwards	69
4-15	Etching and mounting finished sample (a) Image of the sample during etching. The discoloration is remaining titanium on the sample. Continue etching until the entire underlying sample is transparent. (b) Bright-field image of a finished sample which is mounted. Wire bonds are made to deliver MW and DW current to the sample.	70
5-1	An image of a schematic diagram of a spin microscope.	71
5-2	Illustration of the beam excitation path. Light emitted from the laser is expanded by a 10x beam expander. The beam is focused onto the back aperture of the objective. This focused beam is then collimated by the objective.	72
5-3	Figure showcasing the definitions of terms in the thin lens equation. This image was taken from Wikipedia [62].	73
5-4	An image of the optical elements that comprise the excitation path. A Coherent Compass is used as a green laser.	73
5-5	A fluorescence image from NVs that are located within the excitation spot. The black lines superimposed onto the image trace the outline of the microwave wire.	74
5-6	Image of the Signal Generator that delived the MW current. The signal generator is controlled through GPIB by matlab. The emitted MW frequencies are routed through an amplifier and then delivered through the wire shown in Fig.5-5.	74
5-7	An illustration of the collection beam path. Fluorescence from NVs are collected by the objective and focused onto the camera. Stray green light is filtered by a Semrock 532 laser line filter.	75

5-8	Overview of the measurement. The left image is a side view which shows the excitation of NVs and the collection of their fluorescence. The right image is a top view that shows the structure. DC and MW current are run through this wire.	76
5-9	Illustration of a magnetic field generated by the current through a wire. This generation of magnetic field is described by Ampère's law. This image was taken from Wikipedia [56]	76
5-10	Image showing the control devices used to perform the measurement.	77
5-11	ODMR spectra on the electroplated sample (a) ODMR of an NV ensemble when 0mA DC current is run through the electroplated sample. (b) ODMR of an NV ensemble when 60mA DC current is run through the electroplated sample.	78
5-12	Wide-field fluorescence image of NVs on the electroplated sample. . .	78
5-13	Magnetic field image measured by curve fitting the broadened ODMR curve for each NV ensemble in the FOV.	79
5-14	Magnetic field images Magnetic field images measured through sparse sampling. (a) The interval that this image captures is between 0 to 3 seconds. (b) The interval that this image captures is between 9 to 12 seconds.	79
5-15	Summary of the magnetic field images generated from sparse sampling. A-C show the different magnetic images generated from the increasing DC current in the wire. The green dashed lines represent the intervals that the images were averaged over. Image E represents an interpolated magnetic field image at 60mA DC current. The image was generated by fitting the NV's ODMR spectrum.	80

List of Tables

3.1	Curve fitting parameters for fitting an ODMR curve	40
4.1	Overview of the fabrication process for performing liftoff.	55
4.2	Overview of the fabrication process for performing electroplating. . .	67

Chapter 1

Introduction

Isidor Rabi was a professor at Columbia University in 1937 when he discovered the quantum phenomenon that was later named nuclear magnetic resonance (NMR) [40]. NMR is the process by which atomic nuclei in a strong magnetic field absorb and re-emit electromagnetic (EM) radiation. This process changes the magnetization of these systems. By measuring the change in the local magnetic field, the presence of nuclei can be detected. This phenomenon was quickly adopted as a method to study surfaces and substances, but it took an additional thirty years before Raymond Damadian, with assistance from graduate students Mike Goldsmith and Larry Minkoff, first successfully used the technique to non-invasively image a human body([45]). Today, under the name magnetic resonance imaging (MRI), this technique is implemented through the use of strong magnetic fields with large gradients. By sweeping these magnetic gradients such that the local magnetic field changes over a patient and subsequently recording the change in magnetization, the distribution of hydrogen nuclei can be imaged. From this, anatomy can be studied.

This infrastructure was later adopted for functional magnetic resonance imaging (fMRI). Whereas MRI focuses on static images of the hydrogen nuclei present in water, fMRI focuses on dynamic measurements of oxygen concentration through blood-oxygen-level dependent contrast. This ability to image dynamic processes is important for imaging neural activity as shown in Fig. 1-1[61].

fMRI and MRI require an ensemble of spins and high magnetic field gradients

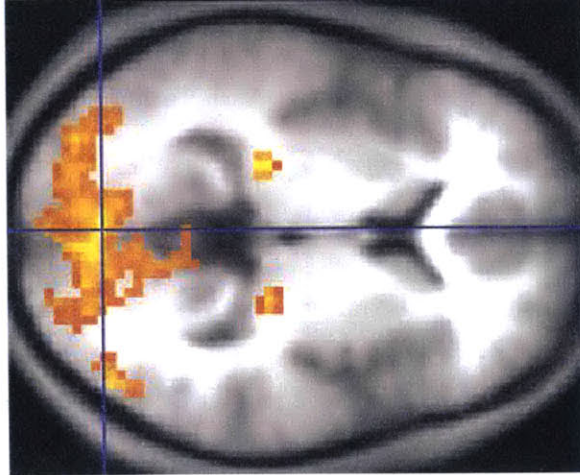


Figure 1-1: Neural Activity captured by an fMRI machine. Taken from Wikipedia [61].

to achieve enough signal to generate an image. Limitations on magnetic coil design makes engineering systems to perform MRI at micron length scales challenging [10]. If magnetic field imaging technology could be extended to the micron length scale and be compatible with biological tissue, then it would allow the direct MRI of cellular systems [47]. Such capabilities would be useful for studying the structure of biological systems.

The nitrogen vacancy center (NV) is one promising candidate to perform MRI processes with a single spin [11] [52] [28] [24] as it emits spin dependent fluorescence [53] and has been shown to have a sensitivity of $4.3 \text{ nT}/\sqrt{\text{Hz}}$ at room temperature[9]. Further, a sampling rate of up to 100 Hz has been shown[48]. The combination of all-optical readout, initialization, high sampling rate and magnetic sensitivity at room temperature makes the NV a possible platform to extend MRI to micron length scales.

In previous work it has been shown that the NV can be placed on the end of an atomic force microscope (AFM) tip to image magnetic fields from stationary magnetic structures [8][54] [43]; however such an implementation has the disadvantage that it can take several minutes to image an area because each point is imaged serially. An alternative technique known as wide-field microscopy, implants a shallow layer of NVs below the surface of a diamond slab and images their fluorescence onto

a camera [51] [23] [13]. This approach has the advantage of parallel readout but is limited to planar geometries. A third approach is to combine wide-field microscopy with NVs in nanodiamonds which are bright, biologically compatible [37] [21] [32], can be attached to complex surfaces[30] [44] and capable of sub-wavelength imaging. Thus, NVs in nanodiamonds are perhaps a natural candidate for serving as robust fluorescent biomarkers of unlimited photostability and low cytotoxicity[47] or imaging biological phenomena. Possible applications include: Monitoring ion concentrations of paramagnetic particles in solution [52], wide-field microscopy in immobilized magnetotactic bacteria [32], precise three dimensional mapping within living systems using nanodiamonds within optical traps [22], nanoscale thermometry [30], and measurements of membrane action potentials. However, NVs within nanodiamonds have properties that vary depending on surface species [29] and suffer from short coherence times [36]. Nanodiamonds are also prone to aggregation which makes the NV's dipole randomly oriented with respect to an applied magnetic field, unlike bulk diamond where NVs have well-defined crystal axes. Thus, performing pulsed sequences or reconstructing an unknown magnetic field from their optically detected magnetic resonance (ODMR) spectrum [51] [35] is difficult. This thesis aims to resolve these problems and further the use of NV ensembles within nanodiamonds for magnetic field and thermal imaging. The rest of this thesis is organized as follows:

In Chapter 2 the NV center is described and its viability as a sensing platform is motivated by discussing its Hamiltonian, spin physics and electronic energy levels. Next, an overview of the experimental setup is given. The chapter ends with an introduction to NVs in nanodiamonds and their biological compatibility is demonstrated.

Chapter 3 introduces NV ODMR models. ODMR curves are fitted to extract parameters that describe an NV system and then those parameters are used to calibrate an external electromagnet. NVs within nanodiamonds are shown to be in disagreement with the previous NV models and instead a new model is introduced that predicts that heavily aggregated nanodiamond NV ensembles diverge in their properties from ideal NV systems. As a result these NV ensembles within nanodiamonds are shown to behave as absolute magnetometers unlike previous models which

predict vector resolution. This model is subsequently used to implement a mapping algorithm to determine the magnitude of a magnetic field through sparse sampling.

In Chapter 4 we fabricate a test magnetic system from microwave strip lines and other structures using liftoff. The Joule heating of these systems is introduced and is shown through thermal mapping. Such thermal heating is not ideal for magnetic sparse sampling algorithms. Alternate fabrication methods, such as electroplating, are introduced to overcome this challenge.

In Chapter 5 a more detailed overview of the experimental setup is given. Ray optics is used to describe optical elements that create a spin microscope. The experiment is described and the results are discussed with the conclusion that the magnetic field from a current carrying wire can be imaged using nanodiamonds at frame-rates greater than 33 Hz across a $10\ \mu\text{m} \times 10\ \mu\text{m}$ field of view.

Chapter 2

Theory and Overview

2.1 General diamond properties

A naturally occurring diamond is composed of 98.9% ^{12}C carbon atoms, with the remaining percentage comprising different carbon isotopes and atomic impurities. Diamond's carbon atoms are arranged in a tetrahedral, face-centered cubic (FCC) lattice as shown in Fig.2-1a[58]. The carbon atoms that make up a diamond lattice are covalently bonded through sp^3 hybridization orbitals. These covalent bonds have a binding energy of 7.3 eV, making diamond the hardest natural material[25]. ^{12}C atoms have a spin neutral nucleus. A diamond composed of ^{12}C atoms acts as a spin free lattice.

Disruptions to the FCC lattice shown in Fig.2-1b commonly arise from impurities found within the diamond crystal. The most common impurity is nitrogen[25]. A diamond can be classified by impurity concentration as follows:

- Type Ia: contains clusters of nitrogen impurities
- Type Ib: contains nitrogen impurities that are distributed throughout the lattice
- Type IIa: contains nitrogen impurities less than 1 to 200 parts per million (ppm)[31]

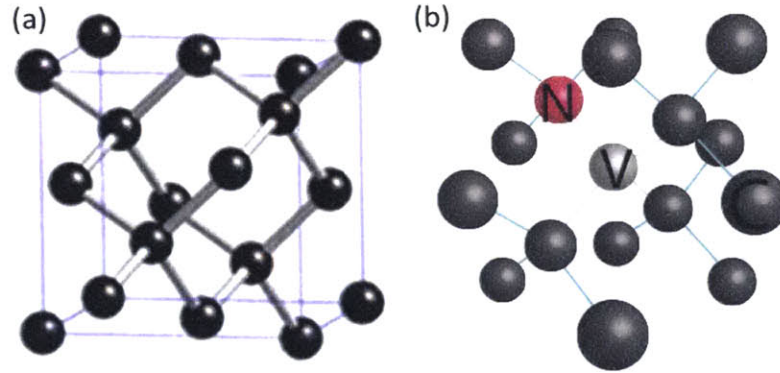


Figure 2-1: **Illustration of an NV center** (a) A model of an FCC diamond. Picture taken from Wikipedia [57]. (b) This illustration shows that an NV is formed when a nitrogen atom (N) replaces a carbon atom (C) and is adjacent to a missing carbon atom. This missing carbon atom is called a vacancy (V). This arrangement is called a nitrogen vacancy center.

2.2 Overview of the Nitrogen Vacancy Center

The nitrogen impurities give rise to an interesting fluorescent crystallographic defect called a nitrogen vacancy center (NV). An NV is composed of a vacancy (missing carbon atom from the diamond lattice) that is adjacent to a nitrogen impurity as shown in Fig.2-1b[12]. This defect exists as two different fluorescent charge states, a neutral NV^0 and an NV^- [26] [50]. They can be distinguished by their spectrum as shown below in Fig.2-2. These spectra have an initial peak which is classified as the zero-phonon line (ZPL). The NV^- has a ZPL at 637 nm and the NV^0 has its ZPL at 575 nm. Both states have broad phonon sidebands that extend into the red from the zero-phonon line. The NV^- spectrum is red shifted compared to the NV^0 spectrum. This allows the two charge states to be spectrally discriminated. The NV^0 does not demonstrate ODMR; therefore its use for MRI processes is limited. Thus, the body of this work will focus on understanding NV^- phenomena and the negative charge notation will be dropped with the understanding that any mention of the NV will be referencing the negative charge state.

The NV comprises 4 electrons of which two are unpaired, yielding an effective spin 1 system [18][15]. The room temperature energy level diagram for an NV is shown in Fig.2-3. This diagram shows several transitions for the NV[18]. The leftmost set

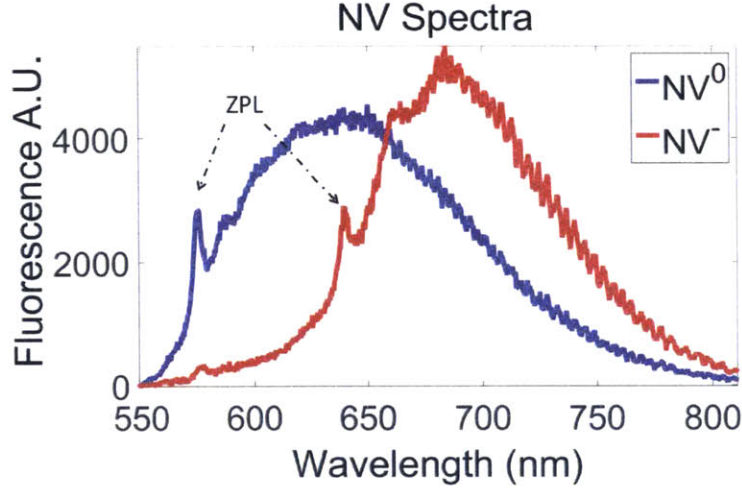


Figure 2-2: The spectrum of the two types of fluorescent NVs. The blue curve is NV^0 and the red is NV^- . NV^- is red shifted compared to the NV^0 allowing for these charge states to be spectrally discriminated. The initial peak is known as the ZPL and it is marked for each spectrum.

of levels (3A and 3E) are the electronic orbital states. These are a triplet ground state and a triplet excited state, respectively. The NV can be excited via a spin-conserving transition into an energy band above the excited state by green light (532 nm wavelength). When the NV relaxes from these vibrational excited states to the vibrational states about the ground state, a continuum of red photons of different wavelengths is emitted. This gives rise to the phonon sideband show in Fig.2-2.

As mentioned previously, the 3A is a spin-triplet ground state, with a $m_s = |0\rangle$ state shown in black and the lifted degenerate spin excited states, $m_s = \pm |1\rangle$, are separated by an energy, E_0 , given by $E_0 = h\delta f = h(2.87 \text{ GHz})$ which results from spin-spin coupling between the two unpaired electron spins [14][39]. The degeneracy of the $m_s = \pm |1\rangle$ spin states can be lifted by applying a magnetic field that has a component aligned with the NV's axis.

There also exists at least one other level labeled 1A between the ground and excited states. Perhaps most crucial is the intersystem crossing between the excited $m_s = \pm |1\rangle$ states and this metastable 1A state which is then followed by a radiative relaxation into the $m_s = |0\rangle$ ground state through the emission of an infrared photon. This crossing has a branching ratio of $\simeq 30\%$.

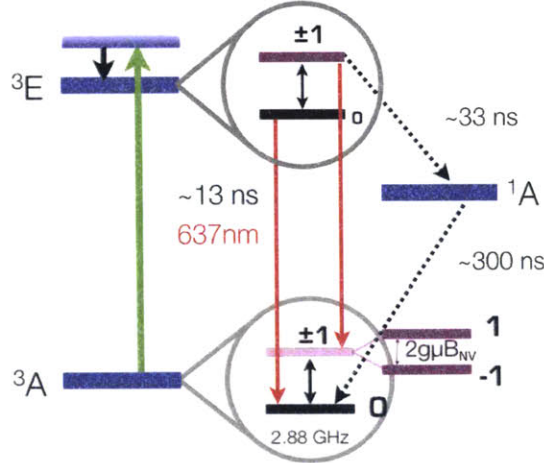


Figure 2-3: Energy level diagram of an NV. The leftmost set of levels (3A and 3E) are the electronic orbital states and are triplet states. The 3A has a splitting of 2.87 GHz between its $m_s = |0\rangle$ and $m_s = \pm |1\rangle$ spin states. These states can be separated by applying a magnetic field that has a component aligned with the NV's axis. The excited $m_s = \pm |1\rangle$ spin states exhibit an intersystem crossing to a metastable 1A level which has a relaxation back to the $m_s = |0\rangle$ ground state through the emission of an infrared photon.

Thus, there are two fluorescence pathways from the excited state. The first is through the zero-phonon line and the associated phonon sideband. This pathway has a lifetime of $\simeq 13$ ns[5]. The other is through the intersystem crossing between the excited $m_s = \pm |1\rangle$ states and the metastable state. This pathway has a lifetime of $\simeq 300$ ns[5]. Since the second transition is not spin conserving, after a few cycles the NV will be, with high probability, optically polarized into the $m_s = |0\rangle$ ground state. The difference in the lifetimes of the pathways means that the measured intensity will differ between these two paths after a few optical cycles.

2.3 NV Physics

The physics of the NV at room temperature can be understood by considering its Hamiltonian [19] which is shown below:

$$H = h (D(T) S_z^2 + E(S_x^2 - S_y^2)) \quad (2.1)$$

where we have neglected the NV's interaction with the nearby nuclear spins and h is Planck's constant, D is the zero field splitting term ($D \simeq 2.87$ GHz) and represents the energy spacing between the $m_s = |0\rangle$ and the $m_s = \pm |1\rangle$ state that was described earlier. The S_x , S_y and S_z are the Pauli spin matrices for a spin 1 system and E is the magnitude of the strain vector along the NV's axis. E represents disruptions in the C_{3v} symmetry of the NV system and is measured in MHz. At room temperature, the D term changes by $\simeq -74.2$ KHz/K [17] as the temperature across the NV is increased. This effect has primarily been attributed to local thermal expansion of the diamond lattice [4].

2.4 NV Interactions with Magnetic Fields

NVs interact primarily with magnetic fields through the Zeeman effect. In the Zeeman effect a spin couples to an external magnetic field through its magnetic moment, $\vec{\mu}$. The strength of this moment is given by:

$$\vec{\mu} = \mu_B \vec{J} / \hbar \quad (2.2)$$

where μ_B is the Bohr magneton and \vec{J} is the total angular momentum of the system. For the NV center, $\vec{J} = 1 \hbar$, so its magnetic moment is 0.014 MHz/ μ T. The total shift is given by:

$$\delta f = g\mu_B \vec{B} \cdot \vec{S} \simeq g\mu_B (\vec{B} \cdot \hat{z} + \vec{B} \cdot \hat{v}_1 + \vec{B} \cdot \hat{v}_2) = g\mu_B (B_{NV} + B_x S_x + B_y S_y) \quad (2.3)$$

where g ($\simeq 2$) is the NV's g-factor, \hat{z} is the normalized unit vector along the NV's axis, \hat{v}_1 and \hat{v}_2 are unit vectors orthogonal to \hat{z} and B_{NV} is the component of the magnetic field along \hat{z} . In the limit of weak magnetic fields ($g\mu_B \vec{B} \cdot \hat{z} \ll D$), the Zeeman effect acts as a small perturbation to the ground state energy. In this limit the NV's Hamiltonian can be modified to include the following terms:

$$H = h (DS_z^2 + E (S_x^2 - S_y^2)) + hg\mu_B (B_{NV} + B_x S_x + B_y S_y) \quad (2.4)$$

where higher-order nonlinear contributions, such as external fields coupling to nuclear species, were neglected. As B_{NV} increases, the splitting shown in Fig.2-4 is observed. This figure shows the location of the NV's resonant frequency as a function of magnetic field.

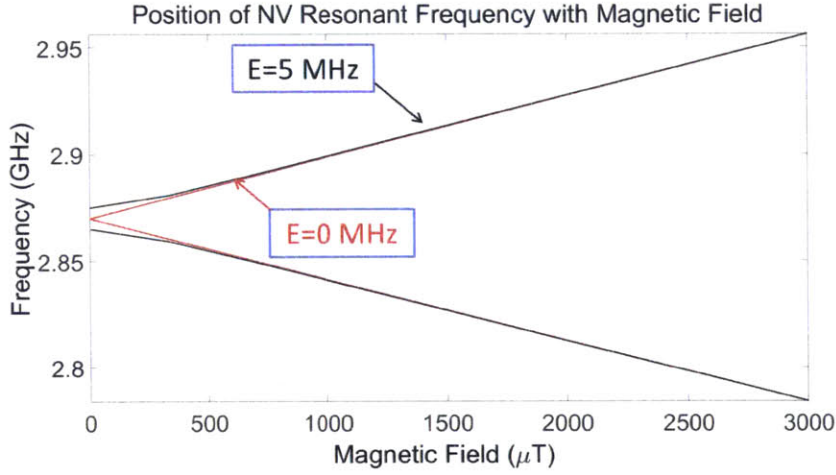


Figure 2-4: Position of an NV's resonant frequency as a function of B_{NV} . The red curve represents an ideal NV system and it showcases a zero field splitting located at 2.87 GHz. The slope is equal to 0.028 MHz/ μ T. The black curve represents an NV within a strained diamond. There is a splitting even at zero magnetic field which is equal to $2E$ [42].

The red curve represents the splitting for an NV in bulk diamond. It starts at 2.87 GHz, which is the NV's zero field splitting, D . For this NV system, as B_{NV} is increased a splitting is observed with a slope of 0.028 MHz/ μ T as explained earlier. However, the black curve represents the position of the NV's resonant frequency when there is a strain across the NV ($E= 5$ MHz in this case). A splitting is seen even at zero magnetic field. The strain reduces the rate of splitting by slightly modifying the NV's Hamiltonian basis such that the actual splitting can be approximated as:

$$\delta f = \sqrt{|E|^2 + (g\mu_B B_{NV})^2} \quad (2.5)$$

2.5 ODMR Measurements for an NV

ODMR is observed when the fluorescence from the NV dips in intensity while applying resonant microwave (MW) fields. As the microwave frequency is swept over the NV's resonant frequency, a drop in fluorescence from the NV is detected. This drop in fluorescence is a result of the resonant driving of the NV's $m_s = |0\rangle$ spin state to the $m_s = \pm |1\rangle$ states. These $m_s = \pm |1\rangle$ states couple to the metastable state resulting in a drop in detected fluorescence. Thus, the NV's ODMR is a result of both the Hamiltonians previously described (where the resonances are located) and the spin selective shelving state of the NV center (the mechanism for the drop in intensity). Simulated ODMR spectra are shown in Fig.2-5a. These curves illustrate how an NV's ODMR changes with B_{NV} . A Lorentzian is seen centered about each resonance frequency as a result of the driving between the NV's two levels [20].

These curves shown in Fig.2-5a are for a single NV. Except by recently developed super-resolution microscopy techniques [12][7], two NVs that are within an imaging system's diffraction limit cannot be resolved[34]. The diffraction limit, d , is calculated from the equation shown below.

$$d = \frac{\lambda}{2NA} \quad (2.6)$$

Where λ is the wavelength of the emission and NA is the numerical aperture (focal length divided by diameter), which is a property of an imaging system. When multiple NVs within the diffraction limit are excited simultaneously, the resultant ODMR curve is the sum of each NV's ODMR spectra. In a bulk diamond there are only four orientations, so a curve similar to the one shown in Fig.2-5b is seen. In this figure, multiple ODMR curve are observed simultaneously, one from each of the NV orientations that exist within a diamond lattice, with one pair degenerate at $D = 2.87$ GHz.

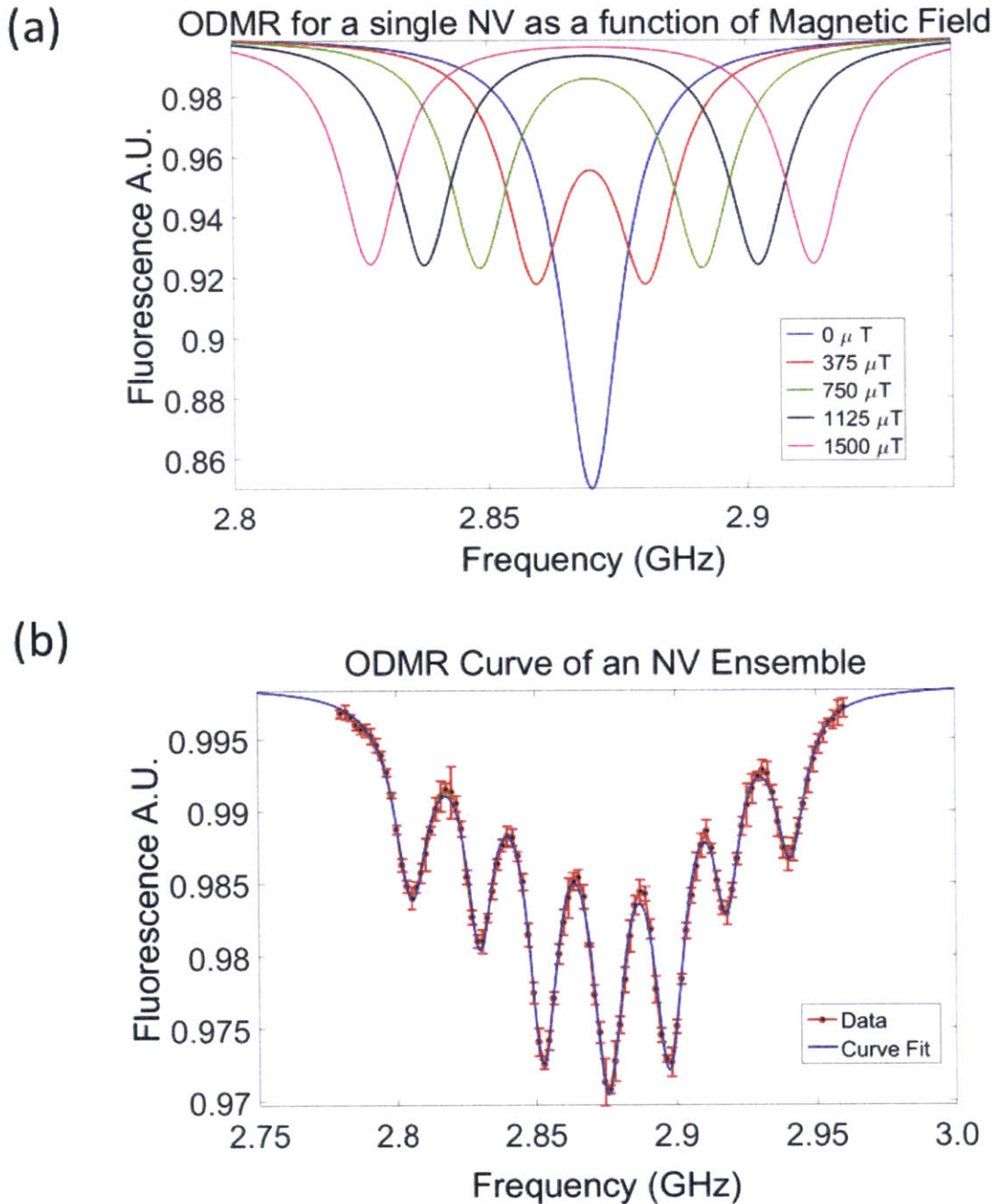


Figure 2-5: **NV ODMR spectra** (a) ODMR spectrum of a single NV at different magnetic fields. These ODMR curves are a combination of the NV's Hamiltonian (where the resonances are positioned), spin selective shelving state of the NV (the mechanism for the drop in intensity) and a Lorentzian which is centered about each resonance. (b) An ODMR of an NV ensemble comprised of all four orientations of the NV within a bulk diamond lattice, with one pair degenerate at $D = 2.87$ GHz. Since the NVs are within the diffraction limit of one another, the measured ODMR curve will be the sum of each orientation's ODMR.

2.6 Magnetic Sensitivity for DC Magnetic Fields

The fluorescence difference for the NV is determined by measuring its fluorescence rate (photons detected per second) when it is being driven on, I_{on} , and off, I_{off} , resonance by MW fields. When this difference is normalized it is called contrast, C , and is defined in the equation below and in Fig.2-6.

$$C = \frac{I_{off} - I_{on}}{I_{off}} \quad (2.7)$$

The sensitivity of a magnetometer is defined as the minimal magnetic field detectable with a signal to noise ratio (SNR) of one. The signal for an NV's magnetic measurement is given by the change in detected photons, given an infinitesimal DC magnetic field variation, δB . For DC measurements, the change in measured fluorescence, γ , is evaluated at the point of greatest slope on the NV's ODMR curve. At this point, a first-order Taylor series can be performed and the change in contrast can be approximated by the following equation. The total measured change in fluorescence for an NV is given by

$$\Delta\gamma = \frac{\delta I_{on}}{\delta B} \delta B \Delta\tau \quad (2.8)$$

In this equation $\frac{\delta I_{on}}{\delta B}$ represents the change in detected photons per second for a shift in δB . $\Delta\tau$ represents the measurement time.

The fundamental limit on the noise of an NV measurement is the quantum noise associated by its spin projections. However in most measurements the predominant noise is photon shot noise[42]. Shot noise is associated with the variation in the detected number of photons[49]. It can be shown that the standard deviation in detected photons, ϵ , increases as the square root of the number of photons detected[49].

$$\epsilon = \sqrt{I_{on}\Delta\tau} \simeq \sqrt{I_{off}\Delta\tau} \quad (2.9)$$

Where we make the approximation that the fluorescence rates on and off resonance are

equal. Combining these results yields an expression for the SNR of a measurement.

$$SNR = \frac{\Delta\gamma}{\epsilon} = \frac{\frac{\delta I_{on}}{\delta B} \delta B \Delta\tau}{\sqrt{I_{off}} \Delta\tau} = \frac{\frac{\delta I_{on}}{\delta B} \delta B \sqrt{\Delta\tau}}{\sqrt{I_{off}}} \quad (2.10)$$

As mentioned previously, the sensitivity, η , is defined as the minimum detectable field with an SNR of one. The SNR can be calculated as shown in the equation below:

$$\frac{\frac{\delta I_{on}}{\delta B} \delta B \sqrt{\Delta\tau}}{\sqrt{I_{off}}} = SNR = 1 \quad (2.11)$$

$$\delta B = \frac{\sqrt{I_{off}}}{\frac{\delta I_{on}}{\delta B} \sqrt{\Delta\tau}} \quad (2.12)$$

The sensitivity is then given by:

$$\eta = \delta B \sqrt{\Delta\tau} = \frac{\sqrt{I_{off}}}{\frac{\delta I_{on}}{\delta B} \sqrt{\Delta\tau}} \sqrt{\Delta\tau} = \frac{\sqrt{I_{off}}}{\frac{\delta I_{on}}{\delta B}} \quad (2.13)$$

We can approximate the difference in $\frac{\delta I_{on}}{\delta B}$ as follows, where δf is the frequency shift of the ODMR curve and w is the full width at half max (FWHM) of the NV's ODMR as shown in Fig.2-6.

$$\frac{\delta I_{on}}{\delta B} = \frac{\delta I_{on}}{\delta f} \frac{\delta f}{\delta B} \approx \frac{I_{off} C}{w} g \mu_B \quad (2.14)$$

Thus, the sensitivity is given in the equation below [42].

$$\eta = \delta B \sqrt{\Delta\tau} = \frac{\sqrt{I_{off}}}{\frac{\delta I_{on}}{\delta B}} \approx \frac{1}{C \sqrt{I_{off}}} \left(\frac{w}{g \mu_B} \right) \approx \frac{1}{C \sqrt{I_{off}}} \left(\frac{1}{g \mu_B \sqrt{T_2^*}} \right) \quad (2.15)$$

For an optimized measurement, where the MW exactly flips the NV's spin from $m_s = |0\rangle$ to $m_s = |\pm 1\rangle$ followed by optical readout [20], the FWHM of the NV's ODMR is approximately inversely proportional to the square root of the inhomogeneous dephasing time T_2^* of the NV center [42]. The T_2^* of an NV center, in bulk diamond, is of order microseconds even at room temperature. This is why the NV is

such a sensitive magnetometer.

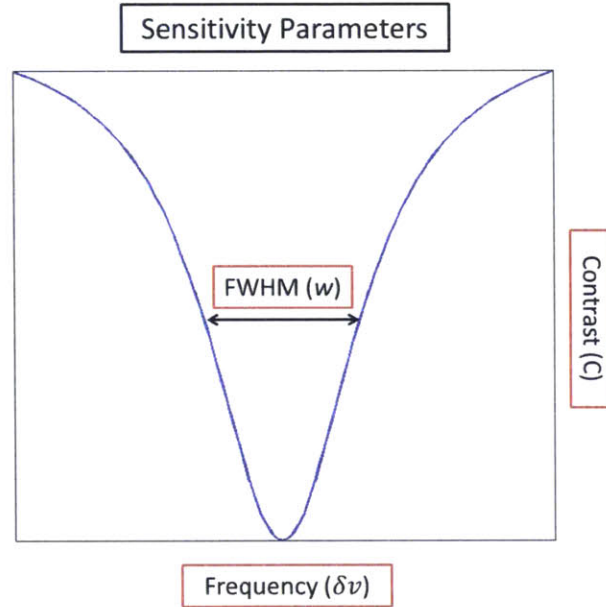


Figure 2-6: Display of sensitivity parameters. FWHM and Contrast are shown for an NV's ODMR spectra.

The properties of the NV can be summarized as follows:

1. The combination of the coupling between the metastable state to the $m_s = \pm |1\rangle$ excited states and the difference in the relaxation rates between the two pathways, results in the NV emitting spin dependent fluorescence.
2. After a few optical cycles, an NV is initialized into the $m_s = |0\rangle$ state, with high probability, through excitation with green photons.
3. The ^{12}C atoms make up a spin-free lattice for the NV. This leads the NV to have a high magnetic sensitivity at room temperature [9].

From the above discussion it is shown that the NV has a high sensitivity to magnetic fields[16] and temperature [38]. When the Hamiltonian shown in equation 2.4 is used the NV's spin state can be determined through its ODMR curve. Previously, a similar process was used on a single NV to detect magnetic fields with a magnitude as little as a $4.3 \text{ nT}/\sqrt{\text{Hz}}$ [9]. Combined with the NV's optical access and ability to

operate at room temperature [42] [36] makes this a promising platform for spin based sensing experiments[24].

2.7 Introduction to the Experimental Setup

To perform magnetic imaging with NVs, the setup shown in Fig.2-7 was built. This setup allows the direct measurement of the NV's spins, which then determines their ambient magnetic field and temperature. In Fig.2-7 it is shown that green excitation light is coupled into the microscope and used to image the NV's fluorescence onto a camera[48]. Thus, every image allows for the parallel readout, within the field of view (FOV), of every NV's spin state[51]. At the sample plane are three solenoids

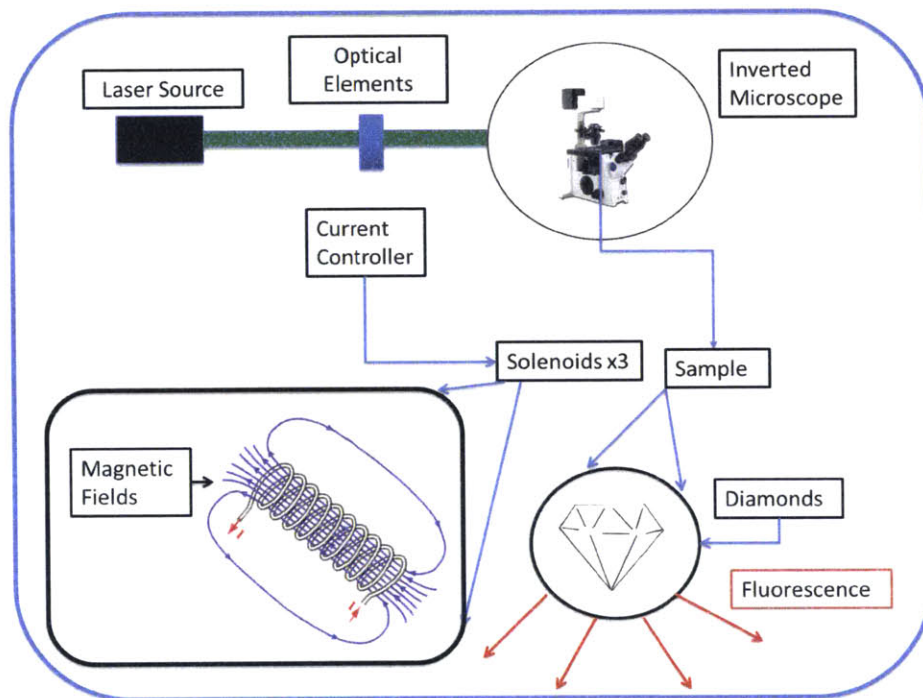


Figure 2-7: An image of a schematic diagram of a spin microscope.

that allow for the local control of the magnetic field.

Once the microscope shown in Fig.2-7 was constructed, a signal generator was added to drive the spins of the NVs through a local antenna using the pulse sequence shown in Fig.2-8. In this sequence, the NV is continuously excited with a green 532 nm laser while applying different microwave frequencies. When the MW frequency

matches the resonance frequency between the NV centers $m_s = |0\rangle$ and $m_s = \pm |1\rangle$ states, a drop in fluorescence is observed. Thus, by implementing the pulse sequence

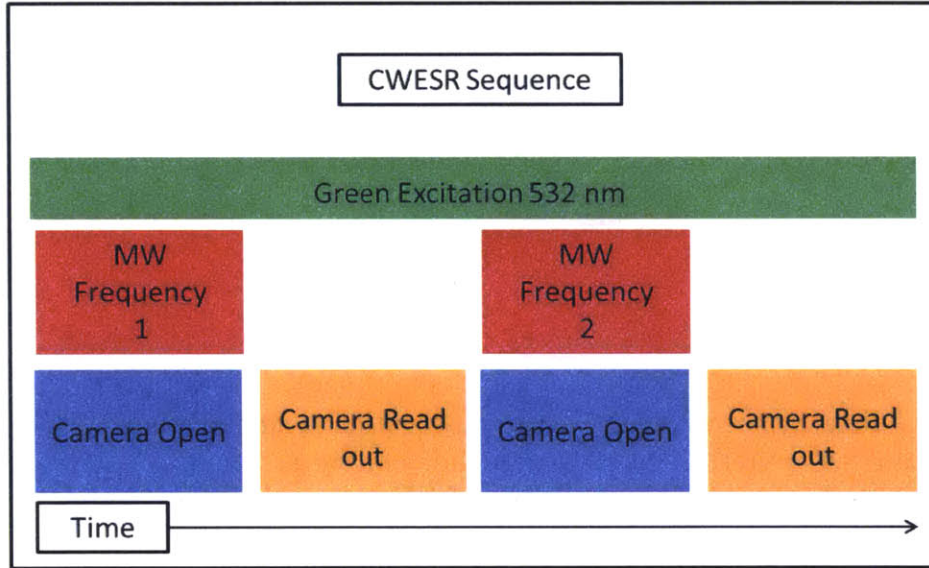


Figure 2-8: CWESR pulse sequence for an ODMR measurement.

shown in Fig.2-8, the positions of the NV's resonant frequencies can be determined. From these ODMR measurements, and using knowledge of the NV's Hamiltonian, the local magnetic field and temperature for each NV can be determined[48]. This method of continuously exciting the NV while performing ODMR is called continuous wave electron spin resonance (CWESR).

2.8 NVs within Nanodiamonds

Up until this point the discussion of NVs has assumed well-defined NV orientations, such as what is found in bulk diamond lattices. However, much progress has been made in fabricating NVs within nanoscale pieces of diamond (nanodiamonds) [30] [33]. These nanodiamonds have been shown to be biologically compatible [30] and have been used as tagging agents for various molecules[32][46]. Further, spin experiments with NVs within nanodiamonds have been conducted in living cells [30]. Fig.2-9 is an illustration of an NV within a nanodiamond with each colored arrow representing an NV orientation. The orientations are each constrained to a diamond's tetrahedral

lattice, but each nanodiamond's lattice can be oriented differently from one another.

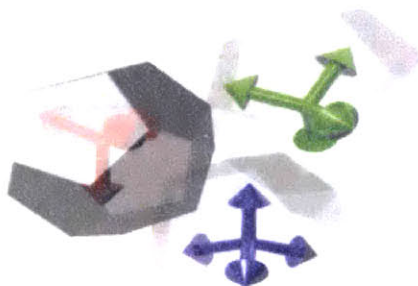


Figure 2-9: Illustration of an NV ensemble within a nanodiamond. Each arrow represents an NV center. The nanodiamonds can be as small as a few nm in size and can contain between one to hundreds of NVs.

In collaboration with Professor Ed Boyden's group, commercially available Adámas nanodiamonds [6] were used to label the surface of a neuron. The nanodiamonds were coated with a thin (1-5 nm) layer of trimethoxy(octyl)silane which was verified by transmission electron microscopy. After coating, the nanodiamonds became hydrophobic.

These functionalized nanodiamonds were stable in toluene. To deliver the hydrophobic nanodiamonds to neuronal membranes, they were encased in micelles composed of phosphoethanolamine conjugated to a PEG group (PEG-PE). These nanodiamonds follow the morphology of the neuron as shown in Fig.2-10. The ODMR from these NVs in nanodiamonds was measured while keeping the neuron alive. The top left image is the white light image of the neuron and the top right image is a fluorescence image of the NVs. Each bright dot is an NV ensemble comprised of nanodiamonds. ODMR measurements were performed on these NVs to confirm their properties as shown in the two bottom images. These results, combined with the NV's high magnetic sensitivity, mean that NVs in nanodiamonds offer the promise to perform highly sensitive magnetic and temperature measurement in living cells.

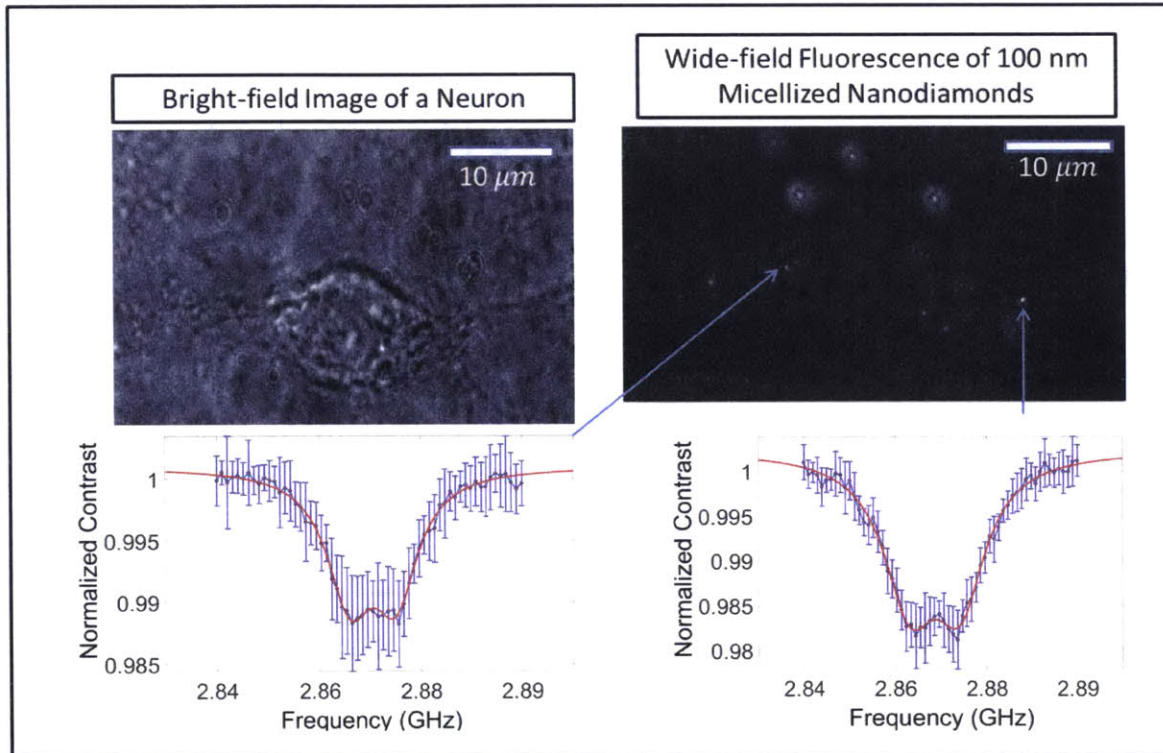


Figure 2-10: **In vitro ODMR measurements of NVs within nanodiamonds attached to neuronal membranes** The top left image shows a bright-field image of a neuron. The top right image shows a fluorescence image of a neuron stained with NV centers. The two bottom images show the ODMR curves from nanodiamonds attached to the neuronal membrane. In vitro ODMR measurements on these attached NVs demonstrate biological compatibility.

Chapter 3

Modeling

3.1 Simulations of NVs with in a Diamond Lattice

Static magnetic field information of the NV's environment is primarily extracted by curve fitting an NV's ODMR spectra. The general overview of this process is shown in Fig.3-1. The ODMR spectrum is fitted and the position of the resonance frequen-

ODMR Curve → Determine resonance frequencies → Extract parameters

Figure 3-1: Fitting workflow to extract sensing information from an NV's ODMR curve.

cies (center locations of the Lorentzians) are determined. These positions determine the NV's Hamiltonian at the time of the measurement. Once the Hamiltonian is determined, the local magnetic field and temperature are backed out. This work flow was confirmed by successfully fitting an ODMR curve of an NV ensemble within a diamond lattice.

A magnetic field was applied across an NV ensemble composed of all four NV orientations within a diamond lattice. To determine the magnetic field's magnitude, direction and the electromagnet's conversion efficiency, ζ , a magnetic field was applied by an electromagnet orientated above the diamond sample as shown in Fig.5-1. We define ζ as the ratio of how much current is converted into magnetic field by the solenoid at the sample plane.

As mentioned previously, the resonance frequency positions need to be determined. These frequencies are the eigenvalue solutions of the NV center's Hamiltonian. Once the resonance frequency for each NV axis has been determined, a specific spectral profile of either a Gaussian or a Lorentzian is assumed to be centered around each resonance. In this case, because a CWESR measurement is being performed, the NVs are MW broadened and a Lorentzian[20] is formed around each resonances according to the equation shown below.

$$F(v, w, f_0, C_i) = \frac{C_i}{1 + \left(\frac{f_0 - v}{w/2}\right)^2} \quad (3.1)$$

where v is the frequency range, f_0 is the resonant frequency, and C_i is the amplitude of the distribution. Summing up the distributions across all the NV orientations results in a simulated ODMR curve. An illustration of this is shown in Fig.3-2. This simulated curve will later be fit to an ODMR spectra to determine the NV's parameters.

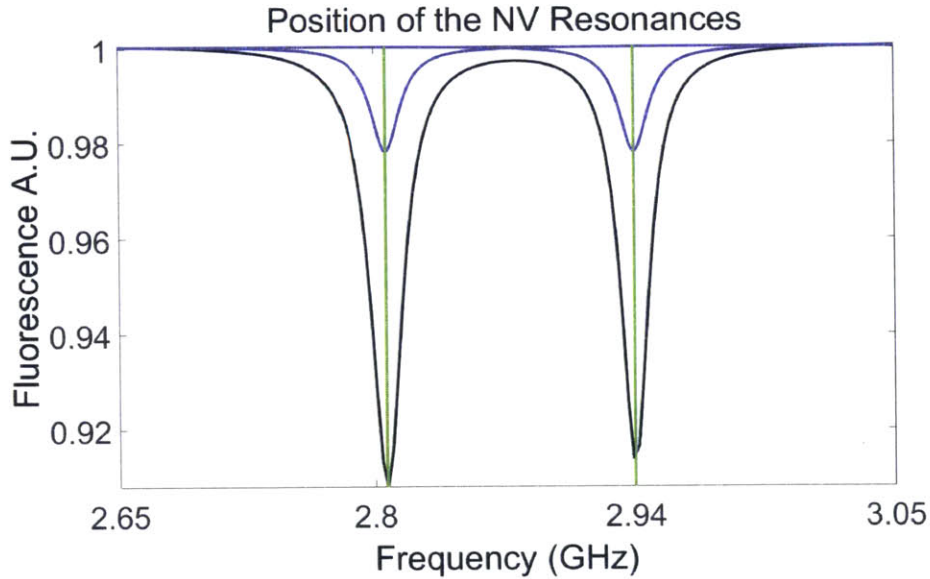


Figure 3-2: Fitting Lorentzians to the NV ODMR's curve. The ODMR curve is the black curve and the Lorentzians are the blue curves. All four NV orientations are degenerate.

To model the magnetic field, four fit parameters were chosen: B_x , B_y , B_z and ζ .

The applied magnetic field vector is modeled as:

$$\vec{B}_{total} = [B_x, B_y, B_z + i\zeta] \quad (3.2)$$

where B_x, B_y, B_z are the applied bias magnetic fields around the setup and i is an input parameter that models the DC current through the solenoid. These last two terms model the applied magnetic field across the NVs from the electromagnet and are defined to be in the z direction.

To model the applied magnetic field's effect on the NV Hamiltonian, the dot product between the magnetic field and the normalized NV axis vector was taken, B_{NV} . To handle the orthogonal magnetic field projections, two orthogonal unit vectors, \hat{v}_1 and \hat{v}_2 , were defined to be centered on the first NV axis as shown in Fig.3-3. B_x and B_y were determined from $B_x = \vec{B} \cdot \hat{v}_1$ and $B_y = \vec{B} \cdot \hat{v}_2$. These unit vectors were then recycled for each subsequent NV orientation by applying the correct rotation matrix between the NV's axes. To handle the lattice and its orientation with respect

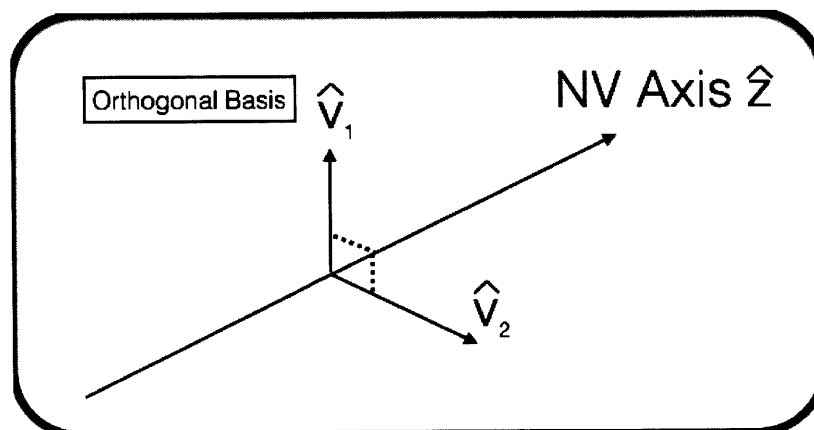


Figure 3-3: Schematic of the orthogonal vectors, \hat{v}_1 and \hat{v}_2 , to the NV axis

to the applied magnetic field, first the vertex points of a tetrahedron are defined as the basis. These are given by:

```
X_0=[1,-1,0,0];
Y_0=[0,0,1,-1];
Z_0=[-1/sqrt(2),-1/sqrt(2),1/sqrt(2),1/sqrt(2)]; % the column vectors...
%... represent the positions in cartesian coordinates
```

```

if first NV axis

basis=NV_axis; % Normalized NV orientation
%compute the rotation matrix
thetay=0;
%% rotation matrix
Rx=[1,0,0;0,cos(thetax),-sin(thetax);0,sin(thetax),cos(thetax)];
Ry=[cos(thetay),0,sin(thetay);0,1,0;-sin(thetay),0,cos(thetay)];
Rz=[cos(thetaz),-sin(thetaz),0;sin(thetaz),cos(thetaz),0;0,0,1];

matrix=Rz*Ry*Rx;

basis=matrix*basis
rand_vec=rand(1,3); %random vector
rand_vec=rand_vec/norm(rand_vec); %normalize
v1=cross(NV_axis,rand_vec); %create first orthogonal unit vector
v2=cross(NV_axis,v1); % create second orthogonal unit vector

end

r = vrrotvec(basis,NV_axis); %determine rotation axis between current...
% ... NV axis and the 1st
m = vrrotvec2mat(r); %compute rotation matrix
B_NV_x=dot(B_vec_iter,m*v1); %apply rotation matrices and compute projections
B_NV_y=dot(B_vec_iter,m*v2);
B_NV_z=dot(B_vec_iter,basis);

```

With this code the NV's axis and its orthogonal basis are recycled for each subsequent NV orientation so that the basis is always consistent. A fit between the simulated ODMR curve and the data is determined by applying a rotation matrix with two fit parameters, θ_x and θ_z . In total, the final list of fit parameters that are

needed are shown in Table 3.1. Where C_1 through C_4 represent the contrast for each

Curve Fitting Parameters			
Linewidth	ζ	Theta.y	Theta.z
B_x	B_y	B_z	D
C_1	C_2	C_3	C_4

Table 3.1: Curve fitting parameters for fitting an ODMR curve

NV orientation. The parameters shown in Table 3.1 are assumed to be constant for any given measurement. Other parameters such as E , are zero for this system and are treated as input parameters.

The simulation requires good initial guesses for the fitting parameters to operate correctly. Modeling the rotation of the crystal was done by applying a strong bias field at 0 DC current to isolate all 8 resonances. An initial guess was generated for the crystal orientation as shown in Fig.3-4a. Once the ODMR curve was fitted, all the parameters shown in table 3.1 were determined and the orthogonal bases were recycled for future fitting. In Fig.3-4b this code yielded a conversion efficiency of $\zeta = -26 \mu\text{T}/\text{mA}$ for the electromagnet.

3.2 Nanodiamond Properties

After simulating NVs located in bulk diamond, NVs in commercially available Adámas nanodiamonds were investigated. These nanodiamonds were deposited onto a number 1 coverslip as shown in Fig.3-5a. The black square highlights one nanodiamond in particular that was analyzed. ODMR curves of this nanodiamond were taken at increasing magnetic fields which resulted in the curves shown in Fig.3-5b through Fig.3-5c).

In Fig.3-5a an ODMR curve of a nanodiamond at low magnetic field ($E > g\mu_B B_{NV}$) is shown. When a $1125 \mu\text{T}$ field was applied across this nanodiamond, then the ODMR shown in Fig.3-5b was observed. The application of magnetic field resulted in a sharp drop in contrast and a broadening of the ODMR curve as seen in Fig.3-5d. This can also be seen in the contour plot shown in Fig.3-6.

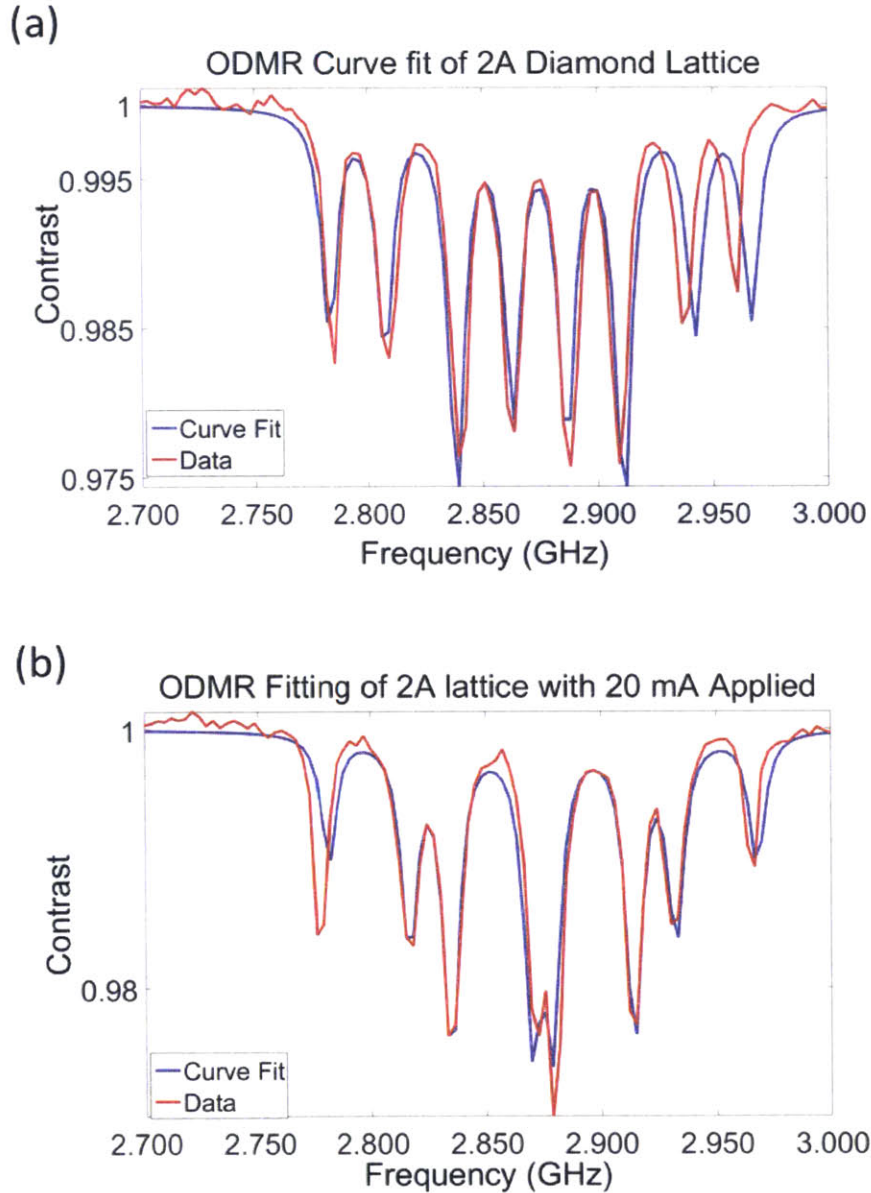


Figure 3-4: **Curve fits of NV ODMR spectra** (a) A large magnetic field was applied to separate all four NV orientations. The ODMR curve was fitted to determine B_x , B_y , B_z and the lattice orientation. (b) The red curve was generated when 20 mA DC current was applied through the solenoid oriented above the sample. The parameters shown in table 3.1 were determined from Fig.3-4a and then recycled leaving only the electromagnet's conversion efficiency at the sample plane, ζ , as the only remaining fit parameter. This parameter was determined from the blue fit. A value of $-26 \mu\text{T}/\text{mA}$ was determined as the overall magnetic field conversion parameter.

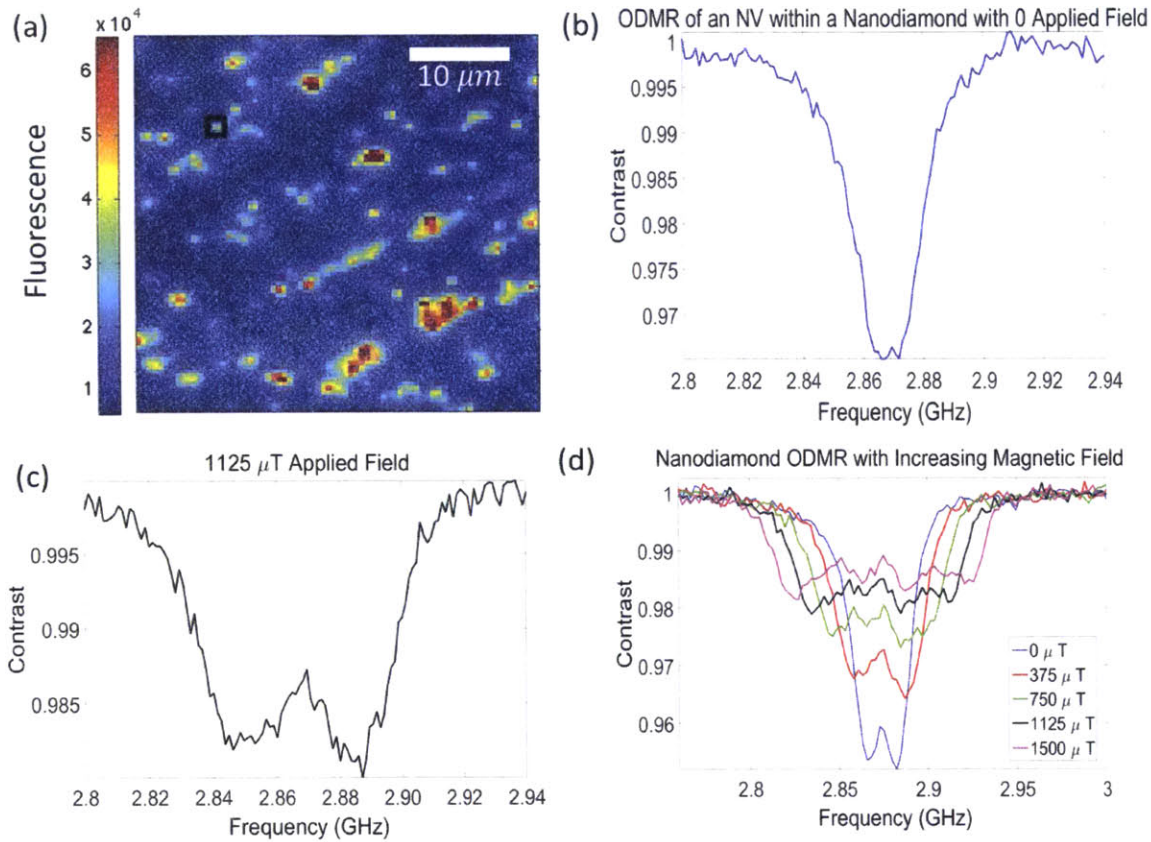


Figure 3-5: **Measured ODMR spectra of NVs within nanodiamond**(a) Fluorescence image of deposited commercially available Adámas nanodiamonds. The ODMR spectra of the selected nanodiamond with increasing magnetic field is shown in figures b-d. (b) ODMR of an ensemble of NVs within the nanodiamond at low magnetic field.(c) ODMR of an ensemble of NVs within a nanodiamond at 1125 μT applied field. (d) ODMR curves of an ensemble of NVs within a nanodiamond measured at increasing magnetic field. Note the drop in contrast and the broadening of the ODMR curve.

This contour plot shows the contrast for an NV ensemble within a nanodiamond over a range of frequencies and magnetic fields.

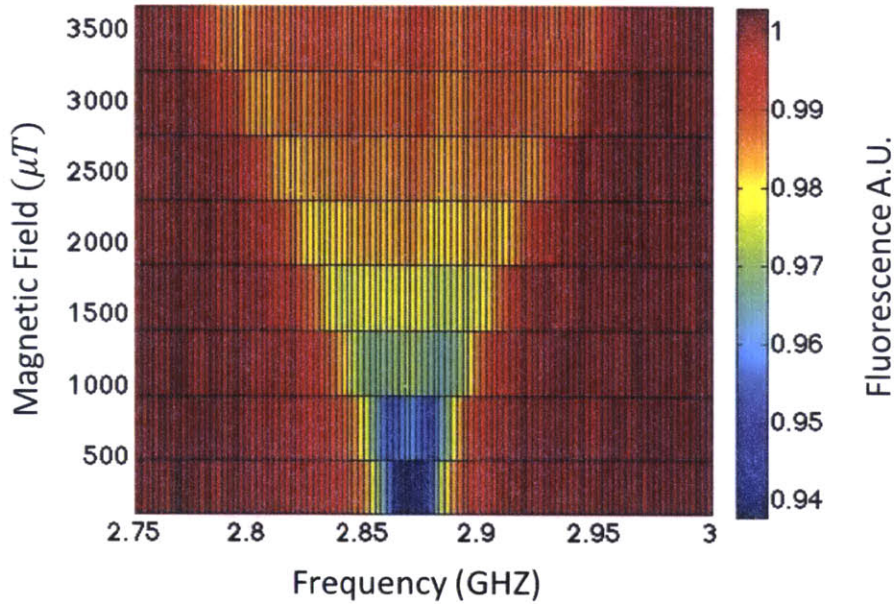


Figure 3-6: Contour plot of the contrast as a function of frequency and magnetic field.

These results are inconsistent with the NV model that was described before. Thus, it became necessary to modify the NV model for bulk diamond systems to describe the effects seen in nanodiamonds.

3.3 NV Polycrystalline Modeling

To explain the above ODMR spectra, this thesis suggest that NVs within aggregated nanodiamonds should be treated as an ensemble of diamond lattices. It has been shown that nanodiamonds can be as small as 2 nm [41]. Thus for the commercially available Adámas nanodiamonds used in this work, this places an upper bound on the number of lattices within a diffraction limited spot. In the limit of many NV lattices within the diffraction limit, NV resonances overlap and are not resolvable. We model such ensembles of diamond lattices as one polycrystalline nanodiamond. A polycrystalline nanodiamond can be idealized as having many NV's orientated around

a unit circle. Each NV is rotated by an angle ϕ and θ about the origin. An illustration of this is shown in Fig.3-7. In a diamond lattice (top image) there are four orientations

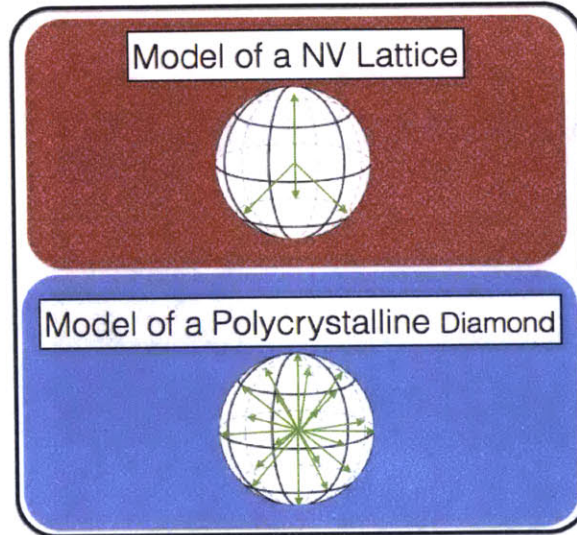


Figure 3-7: **Illustration of two different NV models** The top image shows NVs within defined crystallographic orientations such as those found in bulk diamond systems. The bottom image represents NVs found in aggregated polycrystalline diamond. The NVs are modeled to be spherically symmetrical around an origin.

arranged in a tetrahedron. A polycrystalline model (bottom image) arranges NV's spherically around an origin. Since the NV orientations are spherically symmetric, the applied magnetic field can be treated as being vertically oriented without any loss of generality. As was shown in Fig.2-5b, the final ODMR curve of an NV ensemble of polycrystalline nanodiamonds is the sum of all the contributions of each of the NV orientations. In the limit of many NV orientations within the diffraction limit, the ODMR curve broadens as previously observed because each orientation couples with the applied magnetic field at a different rate. To apply this model, the modeling package for a diamond lattice was reused. An additional for loop ,which loops through all the NV orientations, was implemented.

We can derive an analytical expression for the expected ODMR curve for an NV ensemble within a polycrystalline nanodiamond by considering equation 3.1. This equation describes the expected lineshape about each NV resonance as a function of w and f_0 . Since each NV has two resonances, $f_{0 \rightarrow +1}$ and $f_{0 \rightarrow -1}$ we can expect the

final ODMR curve for a single NV to be equation 3.3. Where the location of $f_{0 \rightarrow +1}$ and $f_{0 \rightarrow -1}$ are given by solving the NV's Hamiltonian.

$$C_{NV}(w, f_0) = A_1[F(v, w, f_{0 \rightarrow +1}) + F(v, w, f_{0 \rightarrow -1})] \quad (3.3)$$

If we now consider the bottom illustration of Fig.3-7 then we can straightforwardly extend this model by integration about the unit sphere. To simplify the calculation, we make the approximation that the driving MW field effects all NV orientations equally.

$$C_{model}(B) = \int_0^\pi C_{NV}(w, f_0) \sin \theta d\theta. \quad (3.4)$$

An additional complication of modeling NVs within these nanodiamonds is that they are strained. To acquire all the parameters that characterize this system, two datasets were taken. As shown in Fig.3-8, a data set at low magnetic field is curve fitted to get the parameters for strain, linewidth, D and C . Once the ODMR curve

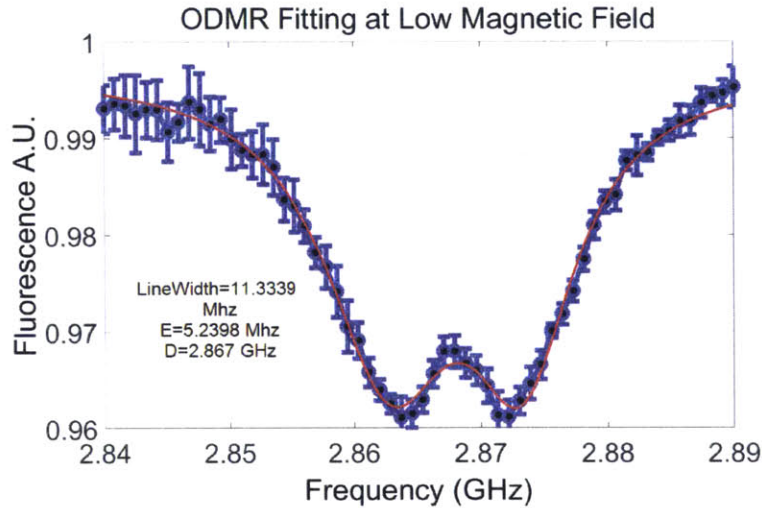


Figure 3-8: ODMR curve taken at low magnetic fields to determine static parameters such as strain, linewidth and contrast.

is fitted, these parameters are recycled for future curves to determine D and B . One NV ensemble was fitted for multiple applied magnetic field values, as shown below in Fig.3-9. From these curves, an estimate for the sensitivity of the nanodiamonds shown

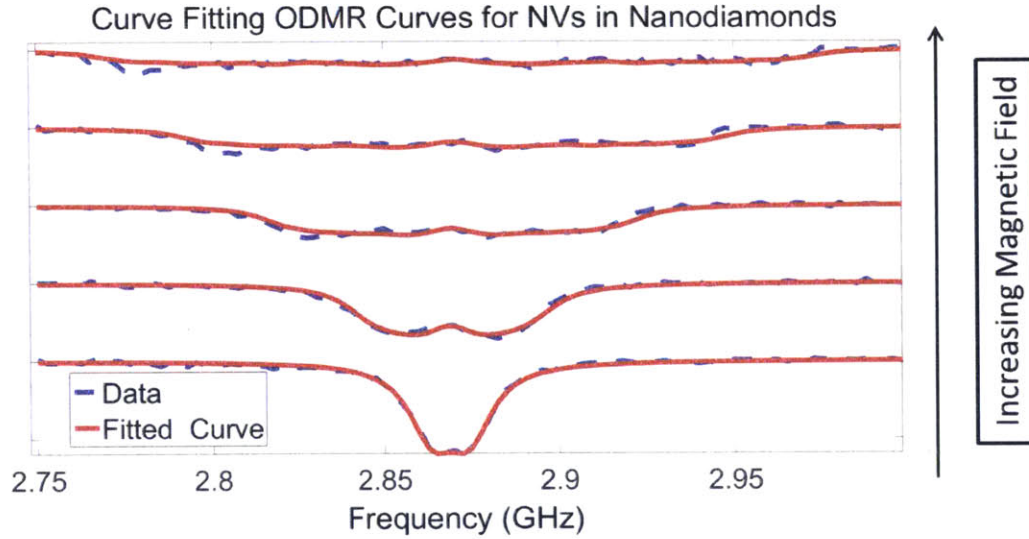


Figure 3-9: Fitted ODMR curves for an ensemble of NVs within a nanodiamond as a function of magnetic field. These result confirm the validity of the polycrystalline model.

in Fig.3-5a can be determined. Fig.3-10 shows a histogram of their sensitivities. A sensitivity better than $2 \frac{\mu T}{\sqrt{Hz}}$ was observed.

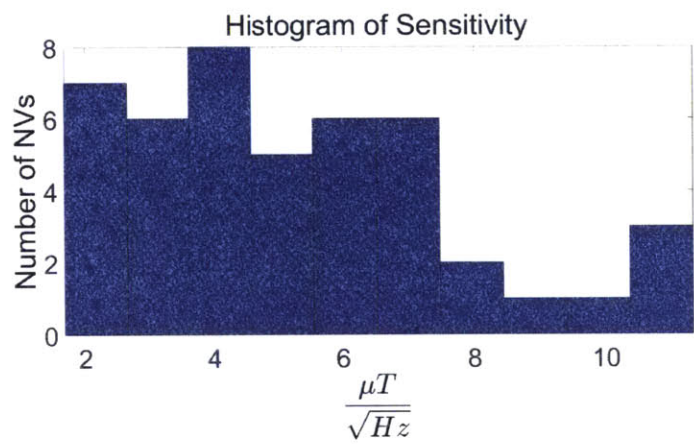


Figure 3-10: A histogram of sensitivity of these aggregated nanodiamond systems.

The drop in fluorescence at one frequency point (2.87 GHz) was observed, as illustrated by the curve shown in Fig.3-11a. This figure is a continuously decreasing function. The reduction in contrast is a result of the NV's resonance frequency shifting with B_{NV} . Unlike in a 2a diamond with fixed orientations, the ensembles' contrast decreases globally with increasing magnetic field. The NVs split incoherently and the

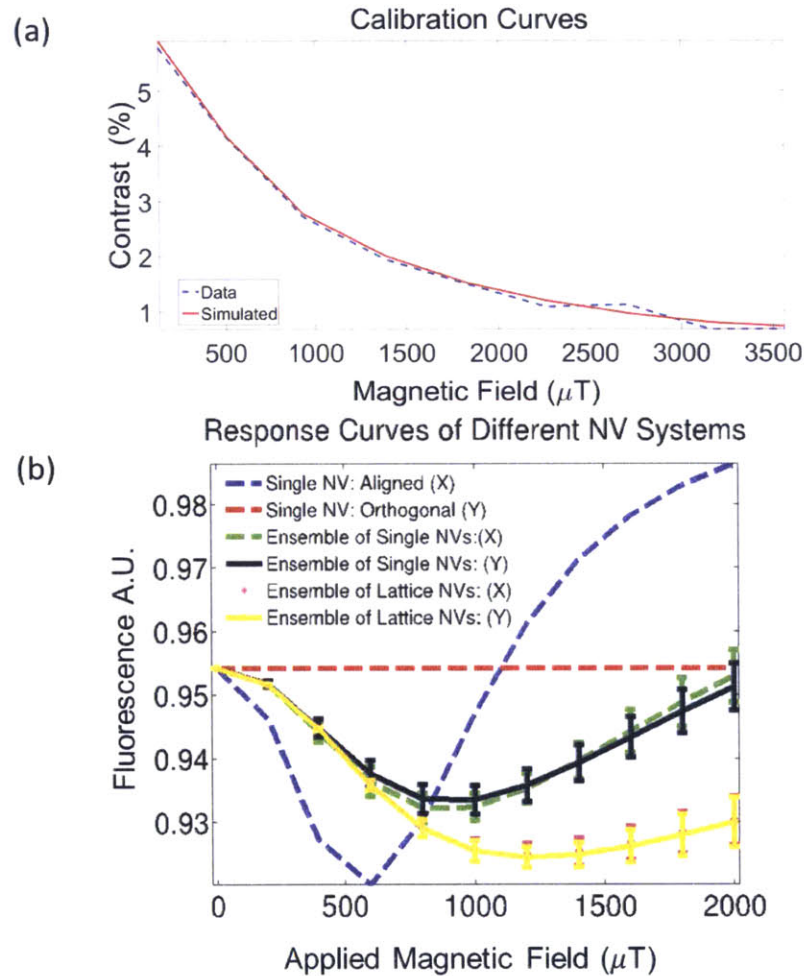


Figure 3-11: **Response curves of different NV systems** (a) Contrast recorded at 2.87 GHz as a function of magnetic field. This is called a response curve. (b) Simulated response curves of different NV systems. It is shown that a single NV has a very different response to magnetic field compared to aggregated ensembles. Error bars on this plot refer to the standard deviation of normalized fluorescence resulting from varying the NV's orientation. The solid curves are the averaged values over all orientations.

SNR reduces as the magnetic field applied across the nanodiamonds is increased. A curve that is plotted like this is called a response curve.

An interesting implication of these polycrystalline diamonds is that their ESR response is independent of the direction of the applied magnetic field. Since the NV's are modeled as spherically arranged around an origin, they respond isotropically to applied magnetic fields. When the direction of the magnetic field is changed, the location of NV resonances are shuffled within the aggregated ODMR envelope but the final resultant curve is unchanged. While this is true for this idealized case of NVs with spherical symmetry, actual aggregated NVs are either one of two cases:

1. An aggregation of single NVs.
2. An aggregation of NV lattices. Each lattice constrains its NVs to one of four possible tetrahedral orientations.

These two cases have different response curves. As shown in Fig.3-11b, the ensembles of single NVs (green and black curves) and lattice NVs (gold curve and pink dots) cannot distinguish, on average, between magnetic fields applied in orthogonal directions (X and Y). The X and Y directions are defined by the reference curves shown for an applied magnetic field aligned with a single NV's axis (blue curve) and a magnetic field that is applied orthogonal to an NV's axis (red curve). A magnetic field that is orthogonal to the NV's orientation does not effect the NV's fluorescence value, yielding a horizontal line as observed. Further, a broadening of an ODMR's lineshape is observed with increasing aggregation. In this figure error bars on this plot refer to the standard deviation of normalized fluorescence resulting from varying the NV's orientation as shown in the bottom image of Fig.3-11b. The solid curves are the averaged values over all of these orientations. In the limit of dense aggregation these response curves for X and Y are indistinguishable. This yields the conclusion that these aggregated NV systems behave as absolute magnetometers.

3.4 Mapping NV Fluorescence to Magnetic Field

Now that a working model has been developed, measured ODMR for NVs within nanodiamonds can be fitted to determine their ambient temperature and magnetic field. Such an approach requires sampling the fluorescence at many frequency points to back out these parameters. A method that allows for the determination of an applied magnetic field from one frequency point would allow for a drastically higher imaging rate of magnetic fields. This requires an accurate mapping of NV fluorescence to applied magnetic field. Using the simulations previously developed, different mapping schemes are compared below. For each of these cases the accuracy of the mapping is evaluated with increasing magnetic field.

The first method of mapping is to treat each nanodiamond as a single NV. The applied magnetic field is aligned with the NV axis. In Fig.3-12 the accuracy of this

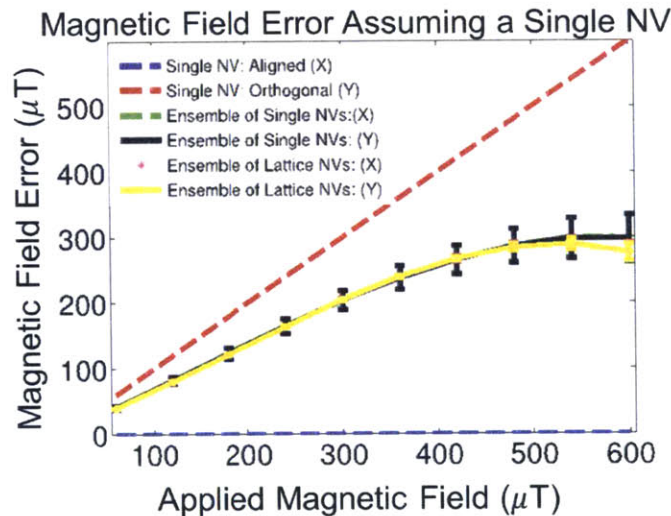


Figure 3-12: Simulated calculation of the magnetic field for different NV systems assuming a mapping based on the response curve of a single NV with increasing B_{NV} . Error bars on this plot refer to the standard deviation of normalized fluorescence resulting from varying the NV's orientation. The solid curves are the averaged values over all orientations.

mapping is demonstrated. The Y axis denotes the magnetic error expected using this mapping for a given applied magnetic field (X axis). The blue curve gives an error of 0 μT for every applied field because this curve has been defined to be true. Similarly

for a single NV that was orthogonal to the applied magnetic field, a straight line with a slope of 1 is observed. The NV does not yield a differential measurement for orthogonal magnetic fields, thus the error is always the applied magnetic field. For NV ensembles (gold and black curves) this mapping is not very accurate. For a 600 μT field, an error of $\simeq 350 \mu\text{T}$ is observed.

An alternate mapping is to assume a first-order truncation where the fluorescence changes linearly with applied magnetic field. The slope for this mapping is evaluated at $w/2$ of the Lorentzian, denoted in Fig.3-13a by the red dashed lines. This mapping

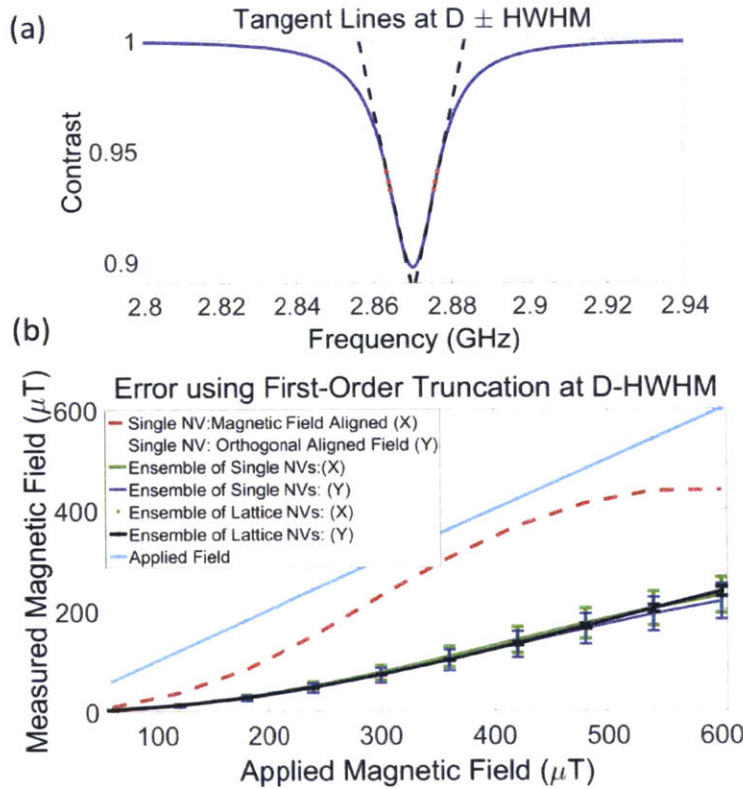


Figure 3-13: **Analysis of first-order truncation mapping** (a) First-order truncation mapping using tangent lines located at $D \pm w/2$. (b) Simulated accuracy of the first-order truncation mapping. This mapping is not ideal for NV ensembles, giving a large error when calculating the magnetic field. Errors greater than $\simeq 300 \mu\text{T}$ across many applied magnetic field magnitudes are observed. Error bars on this plot refer to the standard deviation of normalized fluorescence resulting from varying the NV's orientation. The solid curves are the averaged values over all orientations.

can be mathematically described as follows:

$$\delta B = \frac{\delta I}{g\mu_B m_i} + B_0 \quad (3.5)$$

where δB describes the change in magnetic field, m_i is in units of contrast per frequency and describes the slope of each of the tangent lines shown in Fig.3-13a, δI is the change in fluorescence of the ensemble of nanodiamonds and B_0 is the initial magnetic field across the NV. The accuracy of this mapping is shown in Fig.3-13b.

On the y-axis the calculated magnetic field using this mapping is shown. The light blue dotted line is the applied magnetic field and is shown as a reference. A single NV with increasing B_{NV} gives an error of $20 \mu\text{T}$ and, at worst, has an error greater than $200 \mu\text{T}$. For ensemble systems an error of $\simeq 300 \mu\text{T}$ across many applied magnetic field magnitudes are observed. Thus, this mapping is also inaccurate.

The next type of mapping is based on the response curves for each NV ensemble as illustrated in Fig.3-14a. A mapping is obtained by performing a polynomial fit of the response curve for each NV ensemble in Fig.3-14b. By measuring the fluorescence of an ensemble after calibrating and using this polynomial fitting, the magnetic field across the NV ensemble is determined.

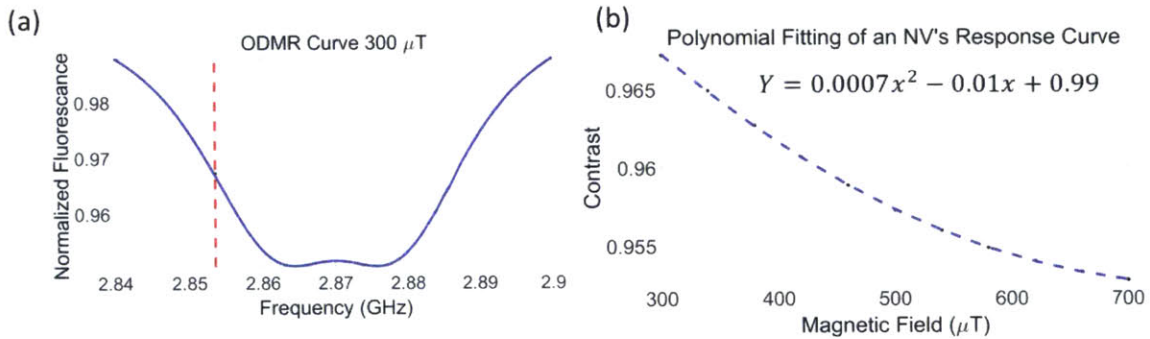


Figure 3-14: **Nanodiamond calibration procedure** (a) Mapping a response curve by sampling the contrast at one frequency point with a known magnetic field value. In this instance the contrast is recorded with an applied field of $300 \mu\text{T}$. (b) The response curve was mapped and fitted to a second-order polynomial. This resulting polynomial is shown above.

Once the fluorescence value is recorded at a given driving MW frequency for

several applied magnetic fields, it is fitted as shown in Fig.3-14b. In principle, the response curves do not have to be measured empirically and can be simulated as shown in Fig.3-11a. Once this mapping has been determined it was tested to sense dynamically changing magnetic fields as shown in Fig.3-15a. Fig.3-15a shows that

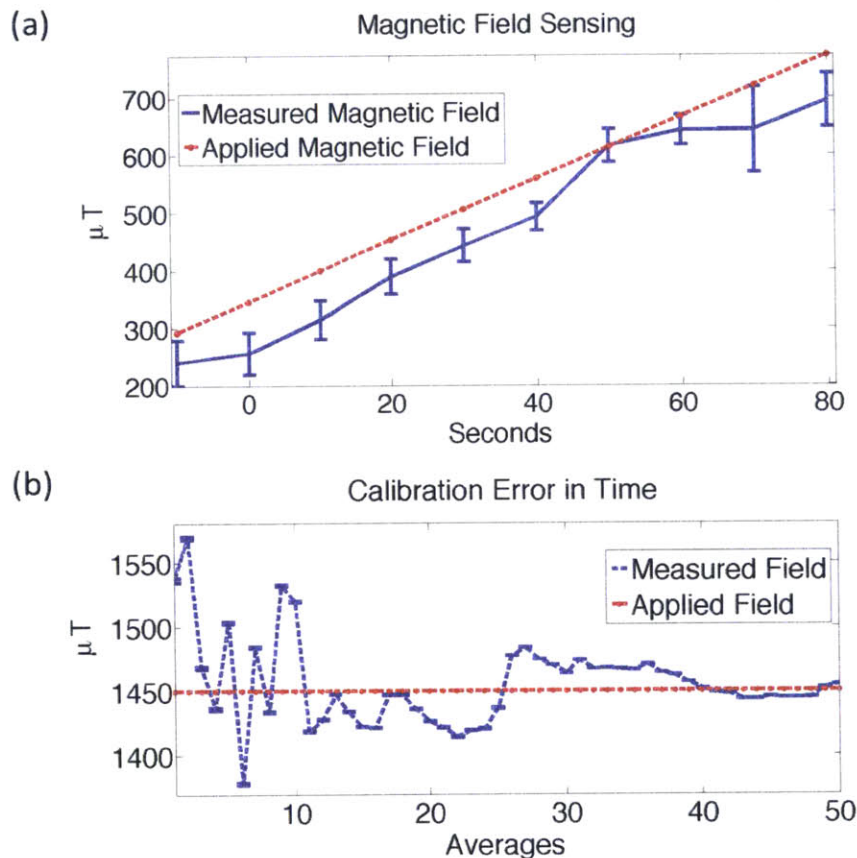


Figure 3-15: **Accuracy of calibration procedure** (a) This calibration method of fitting an NV ensemble's response curve is used to sense a changing magnetic field. (b) The accuracy of fitting an NV ensemble's response curve to sense magnetic field is shown as a function of $\Delta\tau$. Increasing the measurement time reduces the error before the accuracy settles to some systemic error.

a changing magnetic field can be tracked with an average error $\simeq 50 \mu\text{T}$ using this calibration method.

This method of mapping results in a systemic offset from truncating the polynomial fit. For example, the polynomial fitting shown in Fig.3-14b is only a second-order fit. The error results from mapping to a point which does not lie on the response curve. This systemic offset error improves with increasing measurement time, $\Delta\tau$,

before settling to some value that is offset from the NV ensemble's response curve as shown in Fig.3-15b. In this case the red dashed line represents the magnitude of the applied magnetic field and the blue curve represents how the accuracy of the mapping scales with integration time. As the measurements become longer the blue curve gets closer to the red line, oscillates about it, before settling at some systemic offset.

Chapter 4

Fabrication

4.1 Liftoff

Once a model that described NVs within nanodiamonds and maps their fluorescence to magnetic field was developed, it became necessary to develop a magnetic test system. The magnetic field generated by a current carrying wire fabricated onto a # 1 coverslip is such a system. The coverslip was chosen as a substrate because it is index matched with objective oil. The microscope objective shown in Fig.2-7 are coverslip corrected and thus require # 1 coverslips to focus an image.

The first attempt at fabricating this structure used a process called liftoff. The fabrication outline shown in Table 4.1 describes the process for performing liftoff. Performing liftoff on # 1 coverslips is difficult because they are composed of a thermally insulating brittle glass substrate (thickness $\simeq 200 \mu\text{m}$). This low conductivity means that new procedures need to be developed to perform liftoff on them.

4.1.1 Photolithography

As shown in Table 4.1, the first step is to perform photolithography on the substrate. Photolithography is the process where a light sensitive film (called resist) is exposed to ultra violet (UV) light through a masking layer. Regions of resist that are exposed to the UV light undergo a chemical reaction and can later be removed in liquid solution




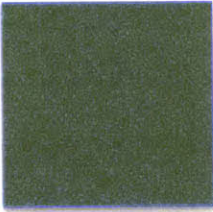
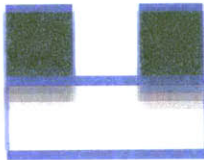
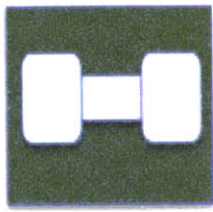
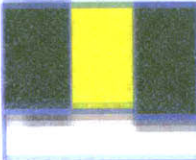
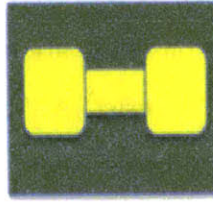
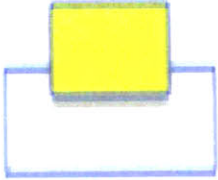
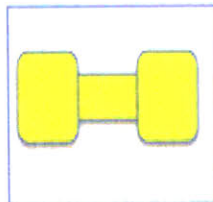
Fabrication Overview of Liftoff Process		
Side View	Top View	Step Overview
		Solvent clean substrate.
		Spin on resist.
		Expose and develop resist.
		Deposit adhesion layer, then a gold layer.
		Strip resist.

Table 4.1: Overview of the fabrication process for performing liftoff.

(developer). Areas that are covered by the mask are not exposed and therefore develop much slower. In this way, designs from a masking layer can be imprinted onto resist, as shown in Fig.4-1. This figure illustrates two types of resist: on the left

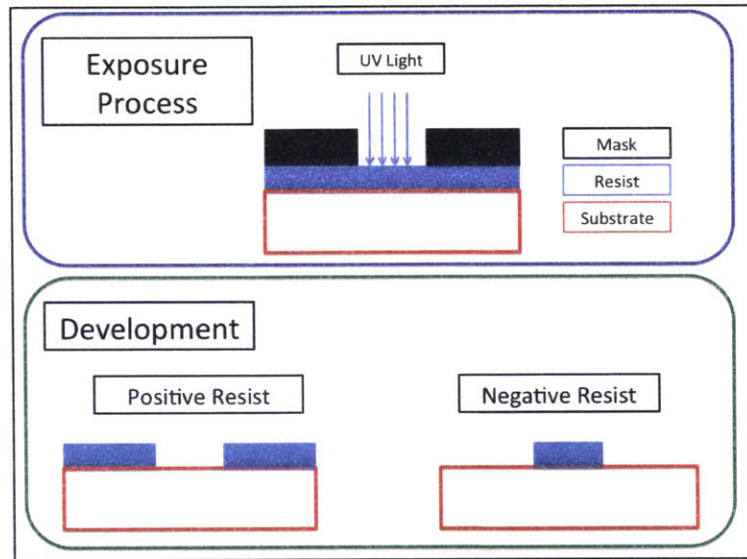


Figure 4-1: This figure gives an overview of Photolithography, where resist is exposed to UV light through a masking layer. Two types of resist are illustrated. On the left is a positive resist and it behaves as described earlier. However, on the right is a negative resist that behaves oppositely. Regions that are exposed harden, unlike a positive resist. In this way, designs on the masking layer can be imprinted onto the resist.

is a positive resist that behaves as described earlier; however, on the right side is a negative resist that behaves oppositely (i.e., regions that are exposed with UV light harden). This procedure will start with a positive resist, AZ5214, and will end with a crosslinked negative resist. Crosslinking is the process where new bonds are formed between polymer chains as a result of illumination. For instance, a positive resist that is initially insoluble in developers becomes soluble as a result of crosslinking through irradiation. This is inverted for negative resists. A crosslinked negative resist is used to ensure correct sidewalls for liftoff as shown in the final sidewall profile in Fig.4-6

The recipe for photolithography that was used is as follows:

1. Clean with acetone and IPA on a spin-coater.
2. Deposit AZ5214 onto the glass slide and run at 3K RPM for 60 seconds. The final resist thickness will be $\simeq 1.5 \mu\text{m}$ [1].
3. Bake at 110 degrees for 2 minutes on a silicon wafer to have good thermal contact with the hotplate (very important). This crosslinks the resist and allows it to

develop as a negative resist.

4. Place in a mask aligner and expose for 5 seconds at 5 mW/cm².
5. Perform post exposure bake again at 110 degrees for 2 minutes.
6. Do flood expose for 45 seconds at 5 mW/cm².
7. Develop in AZ422 for 2-3 minutes or as needed.
8. Dry and check sample on microscope/profilometer.

The first step described above requires the use of a spin coater. Substrates were cleaned and resists were deposited using a spin coater. Solvents were sprayed/pipetted onto the substrate and then rotated at a desired angular frequency as shown in Fig.4-2 [3]. As the substrate is rotated the deposited material flattens and becomes planar.

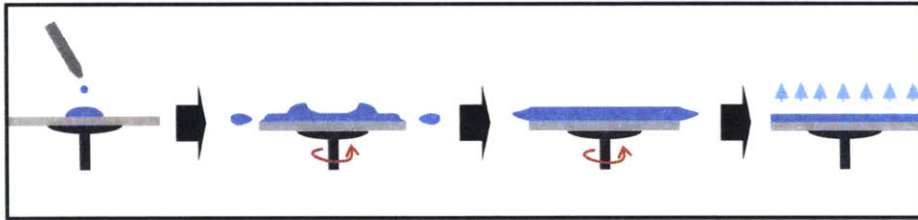


Figure 4-2: A schematic illustrating how a spin coater operates. As the substrate is rotated the deposited material flattens and becomes planar. By varying this speed the resist can be tuned to a desired thickness. This image was taken from Wikipedia [3].

By varying this speed the resist can be tuned to a desired thickness. Once spun for approximately 30-60 seconds, the resist saturates and is now flat. After spinning the resist is now planarized and ready to be exposed in a UV source and developed. Some things to be aware of when spin coating coverslips:

1. Make sure the glass slide has a vacuum seal with the chuck otherwise it will spin off and break. A chuck that is correctly sized to the width of the coverslip is ideal. Avoid squirting solvents into the pump motor.
2. Place the first couple drops from the pipet into the spin coater bowl; these drops have a tendency to dry within the pipet and will coat on poorly.

3. A hot plate is used to remove solvents from the resist. Failure to remove solvents will effect the side wall profile shown in Fig.4-6, which is important for liftoff. Preset the hotplate to the desired temperature and place either an aluminum cup (for small glass slides) or a silicon wafer onto the hotplate as shown in Fig.4-3a. This is done because the glass slides have very little weight and are not in uniform thermal contact with the hotplate. Fig.4-3b is an example of how not to bake a sample. The poor contact with the aluminum foil means their will not be a uniform bake and some regions of the substrate will not crosslink. Thus, the sample will not not develop uniformly. This poor thermal contact will lead to deformities in the final developed sample. Regions develop too much, too little or not at all depending on their thermal contact.

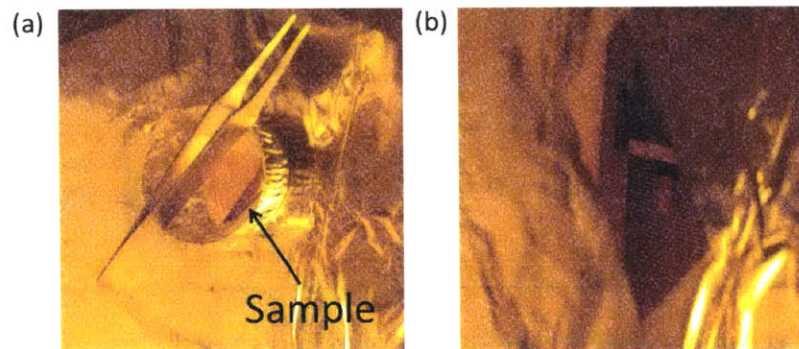


Figure 4-3: **Baking glass slides** (a) A sample is placed in an aluminum cup and weighed down to create a uniform thermal contact between the substrates. (b) Glass slides have very little weight and when placed on an aluminum foil or hotplate, do not have good thermal contact. The poor contact with the aluminum foil means their will not be a uniform bake and some regions of the substrate will not cross link.

4. After baking, expose the resist. First, make sure that the mask (pink side) is facing the sample otherwise the resolution will be poor. Second the product of the exposure time and the bake temperature(s) is what determines how well the sample develops. Increasing the exposure time will increase the development rate, but may hurt the resolution. Increasing the bake time improves the development of exposed regions and preserves resist thickness. However, care should be taken to avoid hard baking the resist. Too much baking, will make

the resist solidify and prevent it from developing.

5. The post exposure bake is what turns the positive resist into a negative resist. After the post exposure bake the exposed regions will cross link and will not develop in solution.
6. The flood expose makes regions of the resist that were not initially exposed soluble in a developer.
7. After developing make sure to check the sample on the microscope/profilometer to confirm that trenches reach the substrate layer. The sample should look like Fig.4-4a.

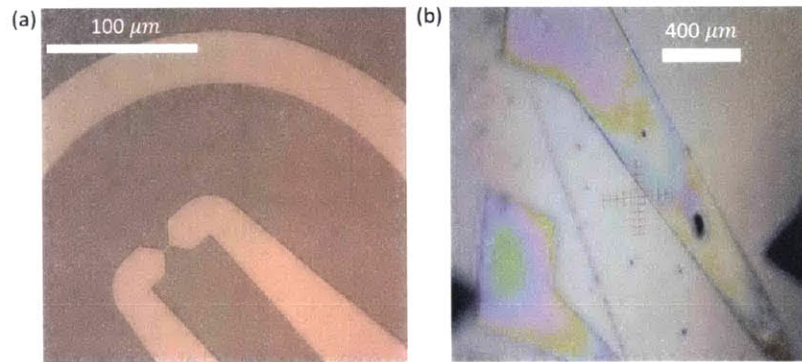


Figure 4-4: **Bright-field images of developed samples** (a) An image of a well-developed sample. A clear contrast between the regions can be observed. (b) An image of an insufficiently developed sample. Large discolorations are a result of thickness variations across the sample.

Fig.4-4a is a bright-field image of a sample post development. A clear optical contrast between the regions can be observed. Any rainbow effects or variations in color (as shown in Fig.4-4b), is a sign that the sample has not been developed enough. These rainbow effects are a result of variations in thickness. These variations are especially prevalent in very large structures, as the internal areas develop slower compared to the areas on the outer edges.

4.2 Electron Beam Physical Vapor Deposition

Now that photolithography has been performed on the coverslips, the samples need to have metal deposited on them. This is done through electron beam physical vapor deposition (EBPVD). An illustration of this process is shown in Fig.4-5 [59]. EBPVD

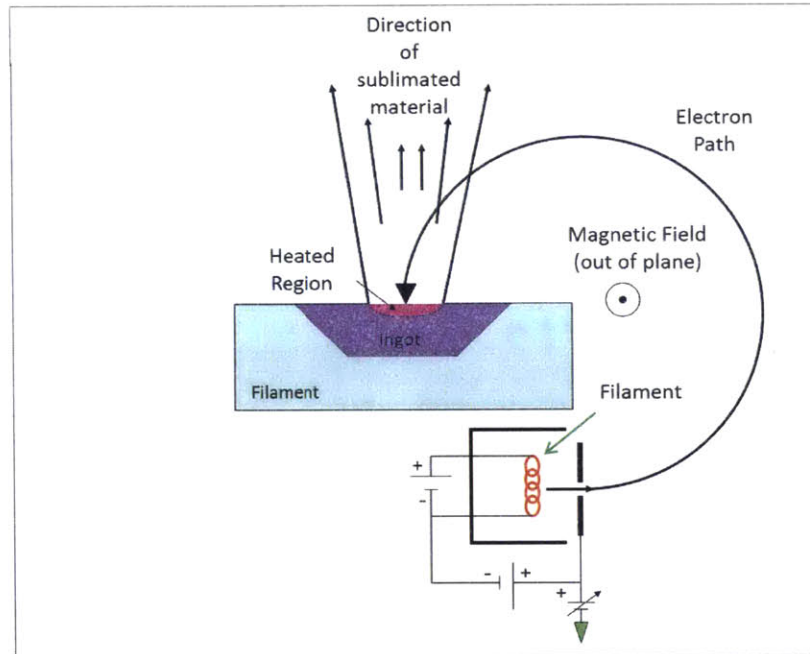


Figure 4-5: EBPVD schematic. Electrons are emitted by a tungsten filament and guided by a perpendicular magnetic field. These electrons impact and sublime the metal in the crucible. This sublimated metal is deposited onto the sample. This image was taken from Wikipedia [59].

is the process where electrons are emitted by heating a tungsten filament. Their kinetic energy (KE) is controlled by DC current through the filament. A controlling magnetic field is oriented perpendicular to the direction of electron emission and is used to control the ejected electrons. These electrons are focused onto a metal crucible which contains the metal to deposit. The metal in the crucible sublimates when the impacting electrons are significantly energetic. This sublimated metal is ejected upward, where a sample is positioned. In this manner by controlling the KE of the emitted electrons from the filament, the deposition rate onto the sample is controlled. For this application, a deposition of an adhesion layer (usually titanium) is deposited first. This adhesion layer is important because it acts as a connection

between the second layer (Au) and the underlying substrate. Without an adhesion layer, gold would not stick to the coverslip. This deposition takes place at high vacuum, because titanium quickly oxidizes into titanium dioxide at pressure greater than 2×10^{-6} torr [2], which is not an effective adhesion layer. Thus, having a very high vacuum is important for the structure's electrical and structural properties.

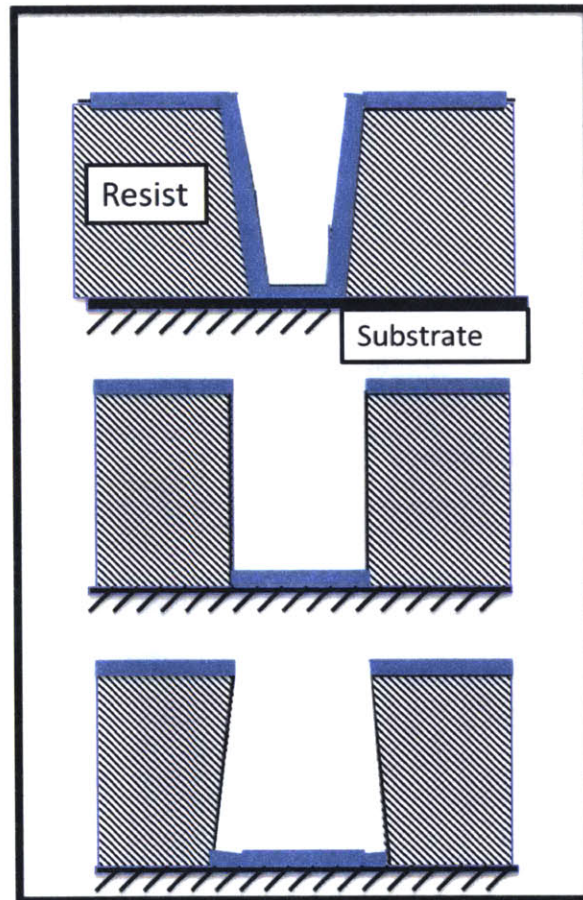


Figure 4-6: Possible side wall profiles from photolithography. The top image is a bad side wall profile. Deposited metal will form metal bridges which can ruin the liftoff. The second profile is acceptable and the third profile is ideal for a successful liftoff.

As shown in Fig.4-6, EBPVD is non-isotropic, because metal is deposited vertically. This is very important because liftoff creates structures by discriminating based on material that is deposited on the substrate and material that is deposited on the resist. As the above figure shows, the blue coloration represents metal depositions. In the first case, material covers the sidewalls as well as the underlying substrate. When the resist is later stripped, a metal bridge between material deposited on the

substrate and on the resist will lead the metal on the substrate to be stripped also. Thus, the top image in Fig.4-6 is a poor sidewall and will lead to a bad liftoff result. The second profile in Fig.4-6 can handle a deposited material to resist thickness ratio of $\simeq 1:5$ or less. The third image can handle a ratio of $\simeq 1:2$ or less. Thus, the second image is an acceptable side wall for the amount of material to be deposited (100 nm), but the third image is ideal. With this kind of angular sidewall, there is very little chance that the deposited material could form a metal bridge. This is why AZ5214 was chosen; after cross linking, it gives the side wall profile shown in image three of Fig.4-6.

Fig.4-7a is the mounting tray for the EBPVD tool. Kapton tape was placed on

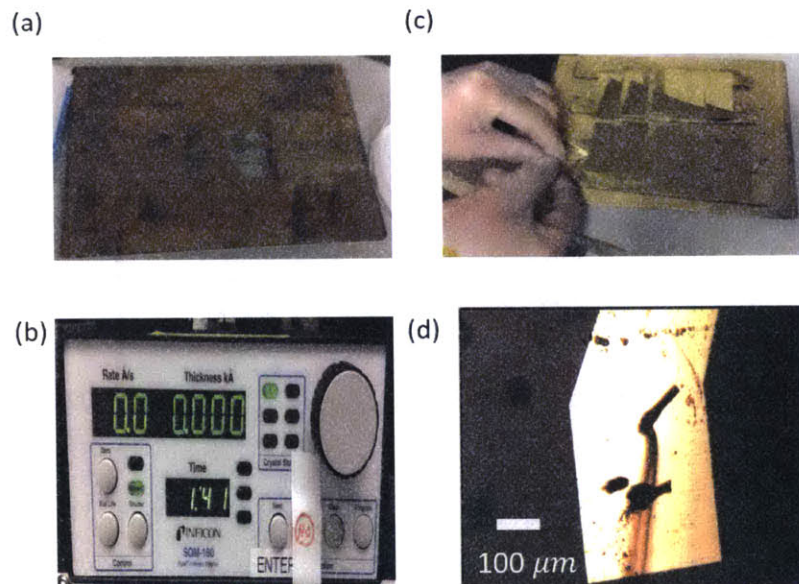


Figure 4-7: **EBPVD procedure** (a) Image of the EBPVD Tray. Avoid making excessive contact between the mounting tape and the glass coverslips. (b) EBPVD pressure sensor and controller. Program deposited material sequentially to correctly calibrate the EBPVD sensor. (c) EBPVD tray post deposition. The entire tray is covered in deposited material. (d) White light image of a completed and wirebonded sample. The gold wire is a wire bond that is bonded off chip. High frequency alternating (AC) current is transmitted through the thick outer wire which generates microwave fields at the location of the NVs. A similar structure will carry DC current.

the metal cover sticky side up, and the glass coverslips were laid on them so that the coverslips remain attached to the tray even while inverted. Only place the corner of the coverslips onto the tape, as the adhesion between the coverslips and the Kapton

tape is very strong. If too much area is in contact, the coverslips are likely to be damaged when removed from the Kapton tape.

Once the coverslips have been mounted and put into the chamber, pump down to base pressure ($\simeq 5\text{e-}7$ torr) and program the materials that are to be deposited into the controller as shown below in Fig.4-7b. After the controller is programmed for the materials to be deposited (in this case titanium and gold), the electron beam gun needs to be activated and aligned onto the first crucible.

Repeat these steps for each metal to be deposited. After finishing, the structures should look like Fig.4-7c, with 100 nm of gold deposited. After EBPVD, the entire tray is deposited and not just the samples. This results in EBPVD being an inefficient deposition process.

Once the deposition is complete, place the samples in a beaker of acetone or N-Methyl-2-pyrrolidone (NMP) to strip the resist. With the correct sidewalls, deposited material that is attached to the underlying substrate will not strip off in solution. A completed structure should look like Fig.4-7d.

In this figure, the gold wire is a wire bond that is attached to a pad off chip. This pad connects to an SMA cable that delivers high frequency alternating (AC) current through the thick outer wire which generates microwave (MW) fields at the location of the NVs. By driving the NV's spins and reading out their spin state with green light, their ambient magnetic fields can be measured. Another pair of wire bonds will be made to the inner pads to deliver DC current that will be imaged with the NVs within the nanodiamonds.

The ODMR curves of NVs within nanodiamonds showed the following effect when the current was increased. The blue curve in Fig.4-8 is an example of an ODMR curve of an ensemble of NV centers at 0 mA DC current. When 20 mA of DC current is applied, the green curve is observed and shows that the resonances have decreased in energy. This effect is characteristic of an NV that is being heated. A decrease in the zero field resonance line (D parameter) is caused by an increase in temperature across the NV center. In this case a temperature shift of 6 Kelvin is observed. To observe the changes in temperature across the nanodiamond ensembles, as the current was

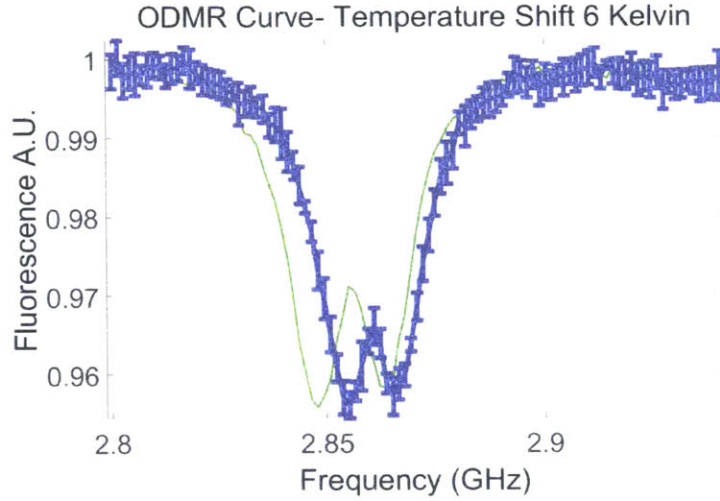


Figure 4-8: Two ODMR curves showing the effects of an increase in temperature of 6 K. Error bars are omitted on the second ODMR curve for clarity.

increased, the D parameter was mapped spatially. See Fig.4-9a (0 mA) and Fig.4-9b (20 mA).

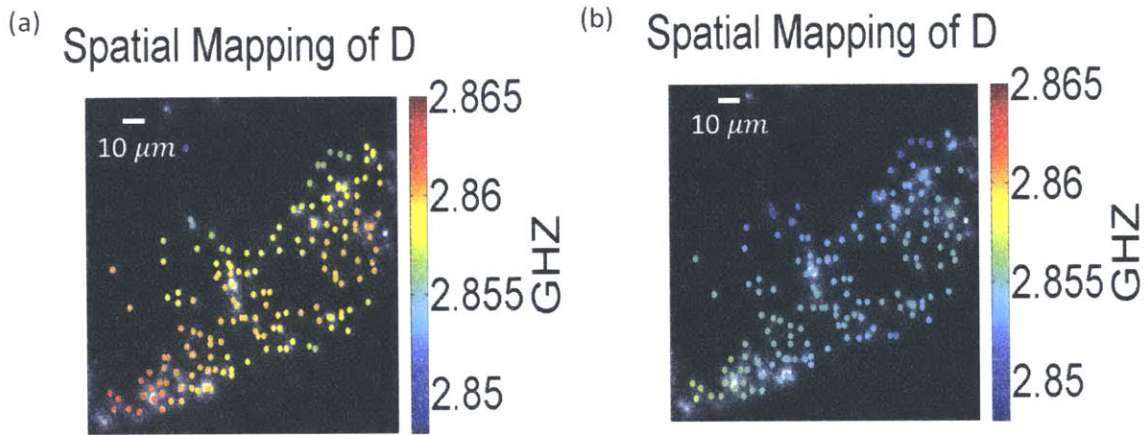


Figure 4-9: **Spatial Mapping of the increase in temperature** (a) D parameter mapping at 0 mA applied DC current through the fabricated structure. (b) D parameter mapping at 20 mA applied DC current through the fabricated structure.

The temperature is shown to increase between the two images because the D parameter decreases for every NV. No ODMR broadening was observed, making this sample unsatisfactory as a magnetic test system. To test the models developed previously, spatially-varying magnetic fields are needed.

The temperature effect can be explained due to high Joule heating caused by the DC current in the wire. Since a reduction in heating is desired, the overall resistance of the wire needs to be decreased. This can principally be done by increasing the thickness of the wire structure. These structures are limited to $\simeq 300$ nm tall because they are made from EBPVD and liftoff. Thicknesses greater than this are in danger of making metal bridges and ruining the liftoff. As shown in Fig.4-7c, deposited material will coat the entire tray. This is very wasteful and expensive. Since significantly thicker structures are needed to reduce heating, a process that only creates materials exactly where desired is ideal. Thus, to increase the thickness by an order of magnitude ($\simeq 1$ micron) a technique called electroplating is more suitable than EBPVD.

4.3 Electroplating

Because liftoff techniques are not ideal for making structures of the desired thickness; electroplating is offered as an alternative. Electroplating is the process where a voltage is applied across a conductive substrate that is placed in a metal ion solution. Due to Coulomb interactions, metal is deposited onto the substrate as shown in Fig.4-10 [60]. As shown, the negative electron charges within the current attracts the positive ions within the solution. This attraction causes the copper ions to deposit themselves onto the metal surface. By increasing the amplitude of the current, the rate of deposition can be increased. Further, where the deposition occurs on the substrate can be controlled by selectively coating some regions in resist. The resist is an insulating barrier that denies the negatively flowing electrons within the metal an interface for interacting with the copper ions in solution. In this manner, the plating rate (by controlling the amplitude of the current) and where plating occurs (by depositing resist) can be controlled. For the structures to be created, the same process will be used, but with gold, rather than copper ions.

With this process, all the techniques previously established to perform liftoff can be reused. The overall process flow for electroplating is shown in Table 4.2. Begin by

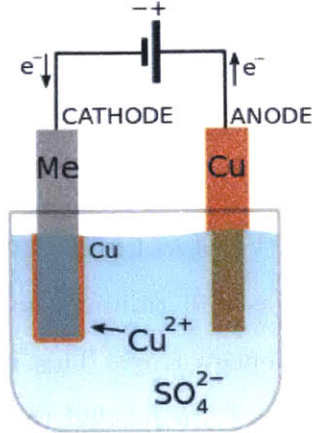


Figure 4-10: A diagram giving an overview of electroplating. A current is run through a metal sample that is placed into a solution of metal ions. The metal ions attach to the surface through Coulomb interactions. This creates a deposition layer. The rate of deposition and the location can be controlled to create structures. This image was taken from Wikipedia [60].

pouring 1200 ml of J.T. Baker's gold electroplating solution and a magnetic stirring rod into a 10000 ml glass beaker. The volume was adjusted so that the sample is completely submerged. Heat the solution to $50 \pm 5 \text{ }^\circ\text{C}$, but do not exceed $70 \text{ }^\circ\text{C}$. This temperature is desired for a constant plating rate. Set the plating parameters on the current controller as shown in Fig.4-11. These parameters are very sample dependent. To visualize the process, think of the sample as a network of parallel resistors. The more plating area (more parallel current channels), the less current that flows in each square unit of area. Some of the samples were tiny and plated at rates greater than $\approx 7 \text{ }\mu\text{m}/\text{min}$. Bigger samples plated at a rate of $\approx 0.3 \text{ }\mu\text{m}/\text{min}$. High plating rates create grain boundaries that increase the structure's resistance. Thus, the DC current



Figure 4-11: The electroplating current controller.










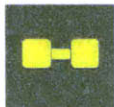
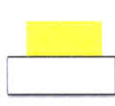
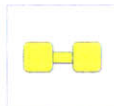
Fabrication Overview of Electroplating Process		
Side View	Top View	Step Overview
		Solvent clean substrate.
		Deposit adhesion layer then gold onto # 1 coverslip.
		Spin on resist.
		Develop resist down to the seed layer and hard bake resist.
		Put the substrate into the solution and begin plating.
		Strip resist and wet etch the seed and adhesion layer.

Table 4.2: Overview of the fabrication process for performing electroplating.

polarity was periodically switched to reduce the depletion region around the plating area and prevents large grains from plating. This creates less grain boundaries. A timing ratio of 20 ms forward current to 1 ms reverse current was chosen.

A slower deposition rate reduces the surface roughness of the final structures. Fig.4-12a is an example of a sample that is plated too quickly (12 mA/min). The height differential between points h_1 and h_2 is calculated by taking the mean value of the curve over the shaded regions. A large amount of surface roughness (> 600 nm) is observed. When the plating rate was decreased to 0.25 mA/min, a smaller surface roughness, as shown Fig.4-12b, was observed ($\simeq 90$ nm). To improve repeatability a dummy load was added to the sample. When a dummy load is included, the area of the structures for each sample is small in comparison to the total plating area.

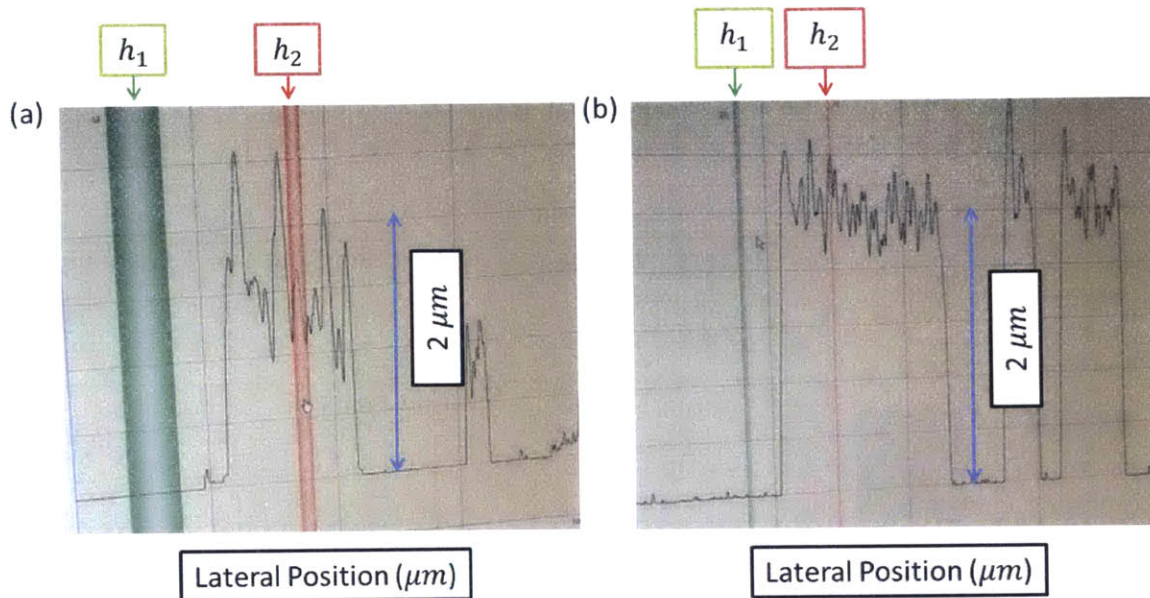


Figure 4-12: **Profilometer measurements on electroplated sample** (a) Sample step profile when structures are plated too quickly. A high surface roughness is observed. (b) Sample step profile when structures are plated slower. A reduction in surface roughness is observed. The height differential between points h_1 and h_2 is $\simeq 2 \mu\text{m}$.

This reduces the variance in plating rates amongst samples. The first attempt was to attach a gold dummy load to the sample as shown Fig.4-13. When clipped to the



Figure 4-13: Image of the sample holder when a sample is clipped in.

coverslips, the samples broke as a result of the brittleness of the substrate. Thus, a thick glass slide was placed as a backstop behind the slides. This insulating barrier between the glass substrate and the dummy load prevents current flow. So a dummy load was added through direct fabrication onto the mask. A finished sample looks

like Fig.4-14a with a sidewall profile shown Fig.4-12b. Fig.4-14b is an bright-field image of the sample after finishing electroplating. Distinct features can be observed. The black particles that cover the structure are nanodiamonds that were placed onto the surface afterwards.

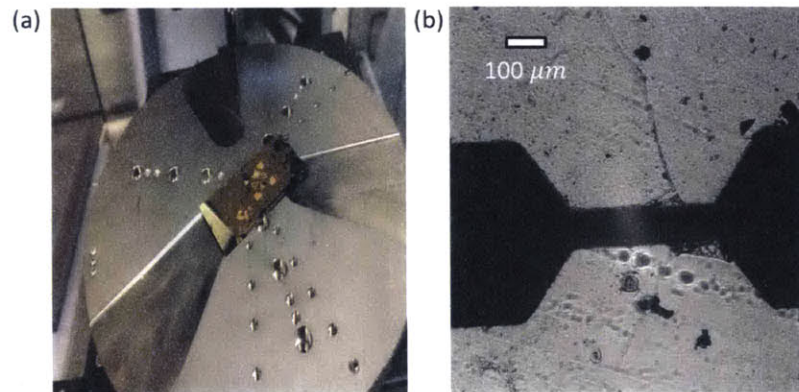


Figure 4-14: **Sample after electroplating** (a) Picture of a finished electroplated sample on the profilometer stage. (b) A bright-field image of a finished electroplated sample. The black particles that cover the structure are nanodiamonds that were placed onto the surface afterwards

After plating, the structure still has a gold seed layer and a titanium adhesion layer. It is necessary to etch away these layer to avoid shorting the circuit. This is done by first stripping the resist layer with acetone. Any resist left on the structure will prevent etching of the underlying seed and adhesion layer, because AZ5214 acts as a masking layer for gold and titanium wet etches [63]. After stripping the resist, place the sample in etchant solution. The first etchant is gold etch TFA and it etches at $\simeq 0.30$ nm per second. For a 100 nm gold seed layer, an etch time of $\simeq 5.5$ minutes is estimated. The etching of the gold seed layer will be complete when the substrate looks silver. This silver coloration is the titanium adhesion layer. After etching in gold etchant, place the sample in titanium etchant TFT. Titanium etches at a rate of $\simeq 0.25$ nm per sec. The titanium etch will be complete when the sample becomes transparent as shown below in Fig.4-15a. The sample's adhesion layer is being etched, revealing the transparent cover slip below. After etching, the sample is mounted to a polychlorinated biphenyl board and wirebonded as shown Fig.4-15b.

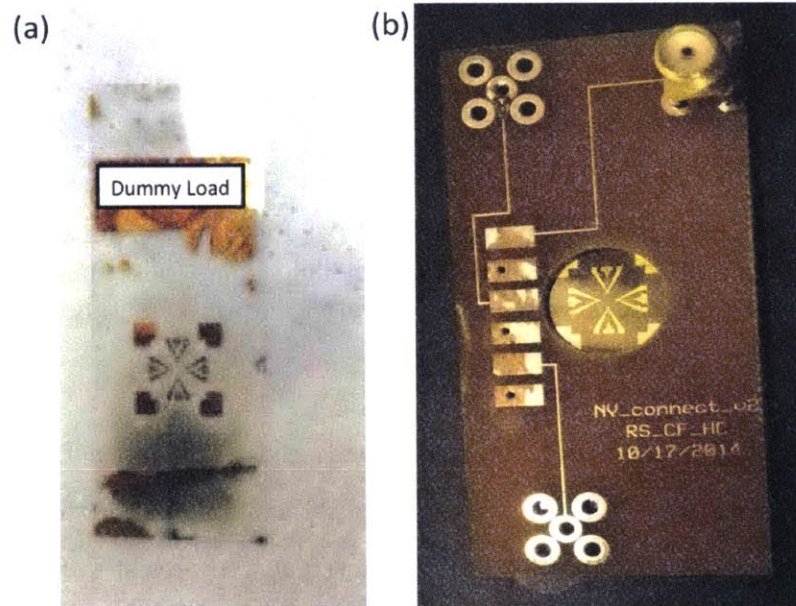


Figure 4-15: **Etching and mounting finished sample** (a) Image of the sample during etching. The discoloration is remaining titanium on the sample. Continue etching until the entire underlying sample is transparent. (b) Bright-field image of a finished sample which is mounted. Wire bonds are made to deliver MW and DW current to the sample.

Chapter 5

Overview of the Experiment and Results

5.1 Overview of Experimental Setup

In chapter 2 an overview of the setup was described. For convenience it is shown again in Fig.5-1. In this figure green excitation light couples into a microscope to excite

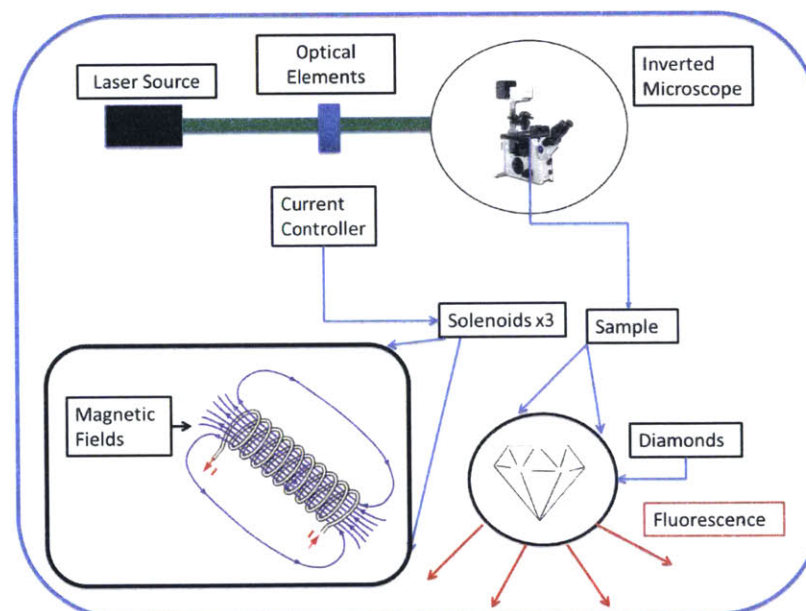


Figure 5-1: An image of a schematic diagram of a spin microscope.

NVs. Light is emitted from a Coherent's Compass laser and the beam is magnified

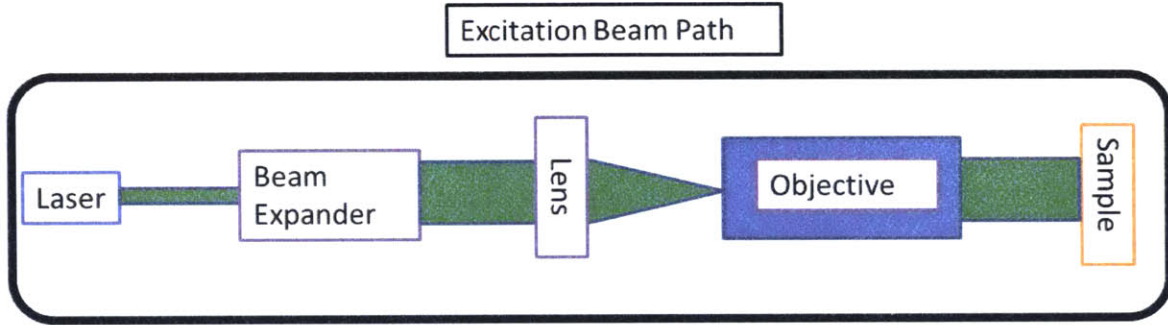


Figure 5-2: Illustration of the beam excitation path. Light emitted from the laser is expanded by a 10x beam expander. The beam is focused onto the back aperture of the objective. This focused beam is then collimated by the objective.

by a beam expander as shown in Fig.5-2. The beam is expanded so that it can be more tightly focused onto the back aperture of the objective. This focused beam is then collimated by the objective.

The exact mechanism for these transformations is known as the thin lens equation [27] and it is shown below.

$$\frac{1}{f_{focus}} = \frac{1}{S_1} + \frac{1}{S_2} \quad (5.1)$$

In this equation, f_{focus} is known as the focal distance of a lens; this is the distance at which incident collimated rays through a lens are focused. S_1 is the object or source distance, and it is defined as the distance from the source of the light to the lens. S_2 is the distance from the lens at which the resulting image is formed. These parameters are shown in Fig.5-3[62]. By convention S_2 is defined as negative when the image forms on the same side as the source. When a light source is very far from a lens, S_1 , the resulting image will be located at f_{focus} . The opposite process is also true: light emitted at the focus of a lens will be projected at an infinite distance away. When light is projected so that it forms an image at infinity, it is called collimated.

It can be shown[27], that the magnification of a lens, M , is given by the equation shown in equation 5.2.

$$M = -\frac{S_2}{S_1} \quad (5.2)$$

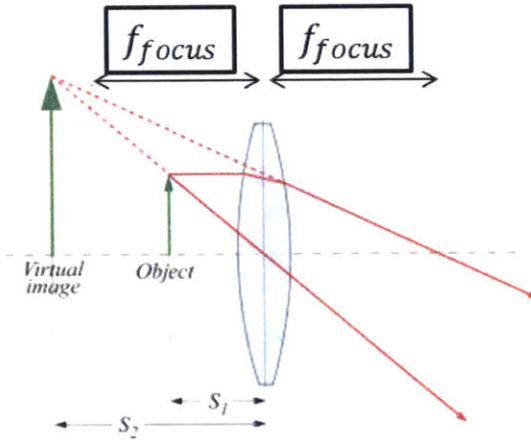


Figure 5-3: Figure showcasing the definitions of terms in the thin lens equation. This image was taken from Wikipedia [62].

From these principals, an understanding of each of the optics described in Fig.5-2 can be gained. The beam expander is comprised of two lenses located a distance apart that is the the sum of f_{focus_1} and f_{focus_2} (the focal lengths of the lenses). When f_{focus_2} is ten times greater than f_{focus_1} the input beam will be magnified by a factor of 10. Further, a magnified beam is more tightly focused by a lens, as the previous equations shows. As shown in Fig.5-2, a focused beam on the back aperture of the objective shows. As shown in Fig.5-2, a focused beam on the back aperture of the objective is emitted as a collimated beam; this can be understood by treating the objective as a lens.

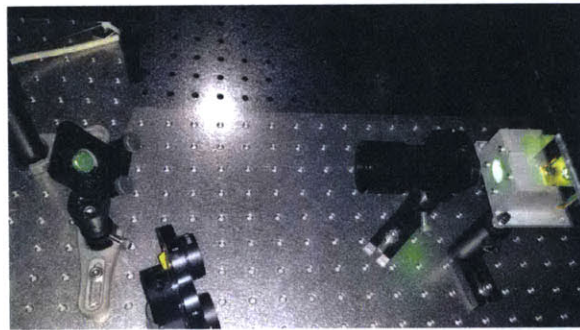


Figure 5-4: An image of the optical elements that comprise the excitation path. A Coherent Compass is used as a green laser.

The light is shaped by the optics shown in Fig.5-4 and is collimated by the objective at the sample plane. It is this excitation beam that allows wide-field imaging to be accomplished. This beam is shown below in Fig.5-5. In this figure a 2a diamond

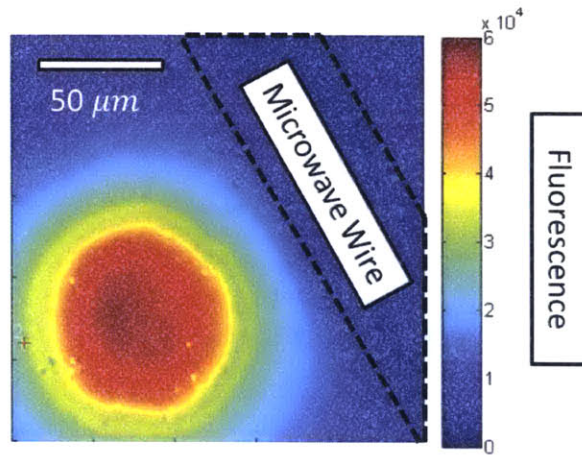


Figure 5-5: A fluorescence image from NVs that are located within the excitation spot. The black lines superimposed onto the image trace the outline of the microwave wire.

slab is excited from the bottom. The fluorescence is emitted by NVs that are within the excitation beam. The black lines superimposed on the image represent the outline of the MW wire that will drive the NV's spin state.

This MW current is emitted from the Rohde & Schwarz signal generator shown in Fig.5-6. This emitted MW current is transmitted by SMA cables (blue chord shown in Fig.5-6). The MW signal is amplified 45 dB by an amplifier. This amplified MW current is transmitted through the wire illustrated in Fig.5-5. By controlling the signal generator, the MW frequencies can be swept through the NV's spin resonances. By correlating which frequency was applied for each collected image, each NV's fluorescence as a function of MW frequency can be plotted. This is how an ODMR measurement is performed.

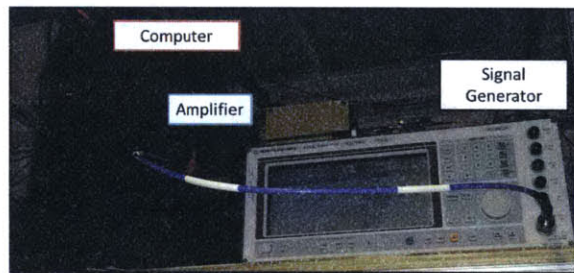


Figure 5-6: Image of the Signal Generator that delivered the MW current. The signal generator is controlled through GPIB by matlab. The emitted MW frequencies are routed through an amplifier and then delivered through the wire shown in Fig.5-5.

Once the excitation beam is coupled through the objective, it excites the NVs located at the sample plane. These NVs emit red fluorescence. The collection path for this fluorescence is shown in Fig.5-7. From the thin lens equation it was shown

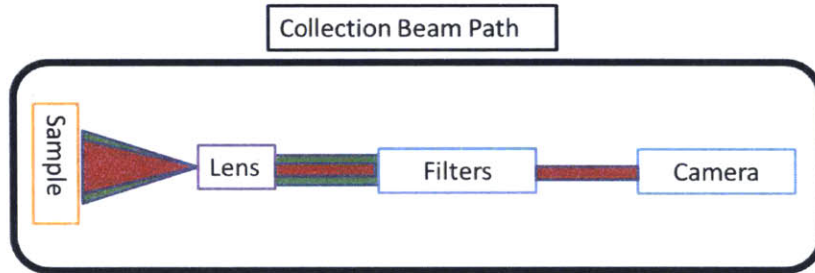


Figure 5-7: An illustration of the collection beam path. Fluorescence from NVs are collected by the objective and focused onto the camera. Stray green light is filtered by a Semrock 532 laser line filter.

that emissions emitted at the focal distance of a lens are transformed into collimated beams. The sample plane is located at the focus of the objective and collimates the collected NV fluorescence. This collected fluorescence is a combination of the fluorescence from the NVs and residual green light from the excitation path. Even though only a small percentage of the excitation light is collected into this path, it still dwarfs the light emitted by the NV. Thus, a Semrock 532 nm laserline filter is inserted. This filter attenuates residual green light and prevents it from reaching the camera so only light emitted by the NV center is collected.

5.2 Overview of the Experiment

In Fig.5-8 a schematic overview of the measurement is shown. On the left side is a cross section of the measurement. Green laser light is shined onto the sample as previously discussed. This excitation light excited NVs within nanodiamonds which emit in the red. The red fluorescence is coupled back through the objective and imaged onto a camera. The right side of Fig.5-8 is a top view of the measurement. This perspective shows that DC current is being run through a wire. This DC current applies a magnetic field that effects the NV's ODMR curve as shown previously. This magnetic field is generated as a result of Ampère's law. In Ampère's law, magnetic

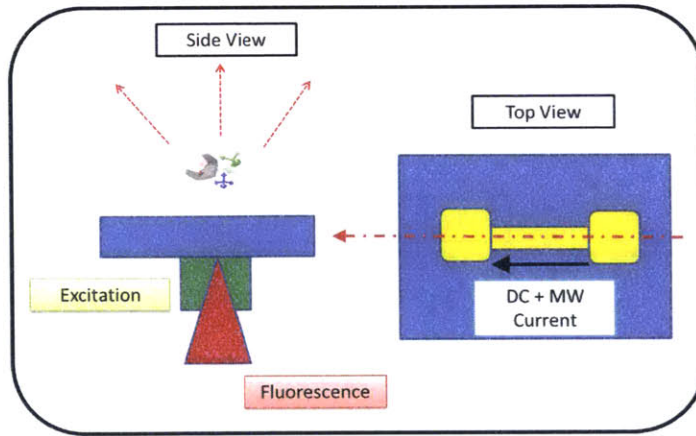


Figure 5-8: Overview of the measurement. The left image is a side view which shows the excitation of NVs and the collection of their fluorescence. The right image is a top view that shows the structure. DC and MW current are run through this wire.

field is generated by current according to the relationship shown in the equation below.

$$\vec{B} = \frac{\mu_0 I_{current}}{2\pi r} \hat{\theta} \tag{5.3}$$

In this equation \vec{B} represents the magnetic field generated by this current and $I_{current}$ represents the current through the wire. The vacuum permeability is represented by μ_0 and r is the distance from the wire as shown in Fig.5-9[56]. From this equation

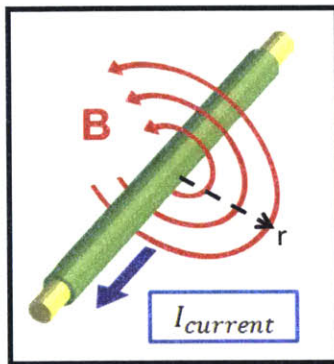


Figure 5-9: Illustration of a magnetic field generated by the current through a wire. This generation of magnetic field is described by Ampère's law. This image was taken from Wikipedia [56]

an understanding can be gained of how the magnetic field changes as a function of distance from the wire.

The current for this measurement is controlled by the equipment shown in Fig.5-10. In the figure, four devices are shown. The rightmost is a Yokogawa programmable



Figure 5-10: Image showing the control devices used to perform the measurement.

current source. This current source is very low noise, and is important for the small magnetic fields that this experiment aims to measure. The Yokogawa is controlled through matlab and the applied current and resistance of the circuit for each measurement is read out in real time. The device to the left of the current controller is a power supply. This power supply drives current through electromagnet coils above the setup. The two left-most devices are multimeters, which record the current through both the electromagnet positioned above the NVs and the wire fabricated onto the sample.

5.3 Experimental Results: Magnetic Imaging

Once the electroplated samples were completed and mounted, the sample was wire bonded. The experiment described above was performed and the ODMR spectrum shown in Fig.5-11a was seen. Running DC current through the sample resulted in the ODMR curve shown in Fig.5-11b. In these figures the contrast decreases as expected for an increasing magnetic field. Curve fitting the ODMR spectrum for every NV shown in the fluorescence image in Fig.5-12 yielded the image showing in Fig.5-13.

Next, the current was increased and the resulting magnetic fields were imaged using the mapping techniques described earlier. These images were produced 101 times faster than those produced through ODMR fitting, where the speed up was a direct

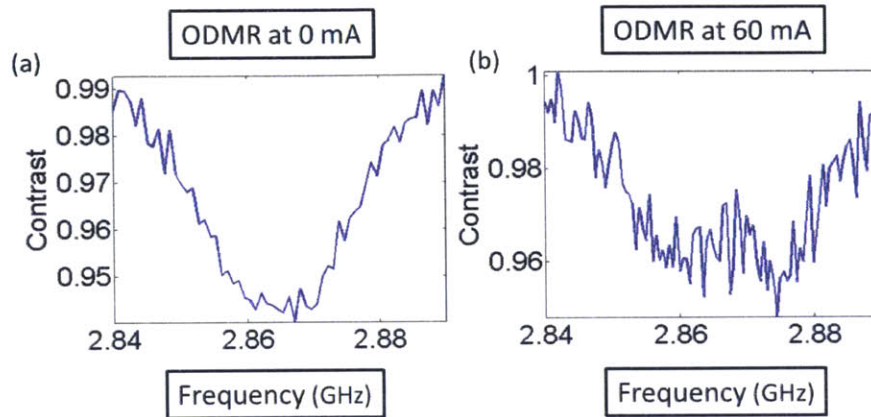


Figure 5-11: **ODMR spectra on the electroplated sample** (a) ODMR of an NV ensemble when 0mA DC current is run through the electroplated sample. (b) ODMR of an NV ensemble when 60mA DC current is run through the electroplated sample.

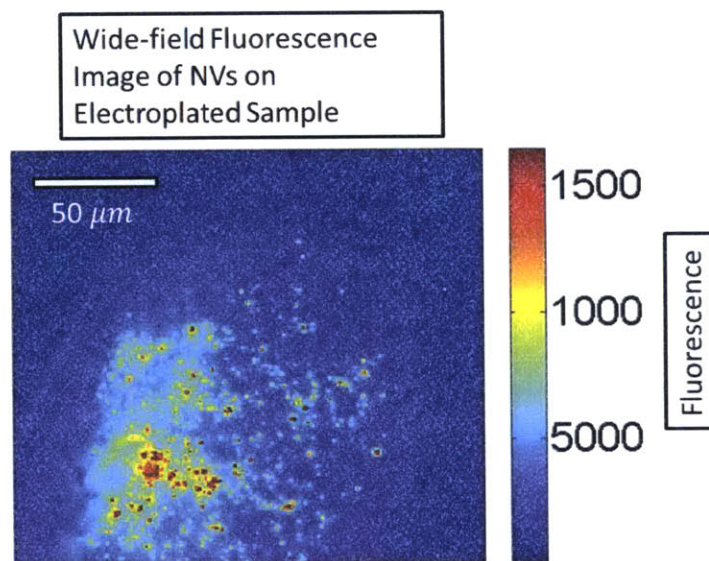


Figure 5-12: Wide-field fluorescence image of NVs on the electroplated sample.

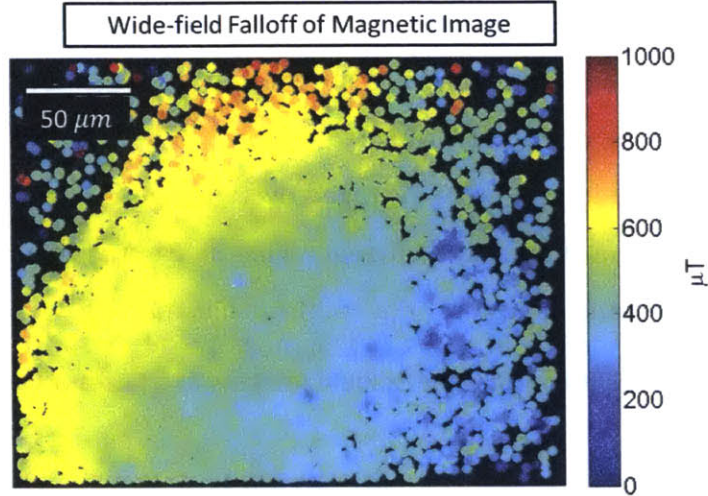


Figure 5-13: Magnetic field image measured by curve fitting the broadened ODMR curve for each NV ensemble in the FOV.

result of the decrease in frequency points sampled. With this mapping the magnetic field was imaged every 30 ms resulting in a framerate greater than 33 Hz. Averaging 50 images together increased the SNR of the resultant image. These averaged images are shown below in Fig.5-14a and Fig.5-14b. Fig.5-14a shows the averaged magnetic

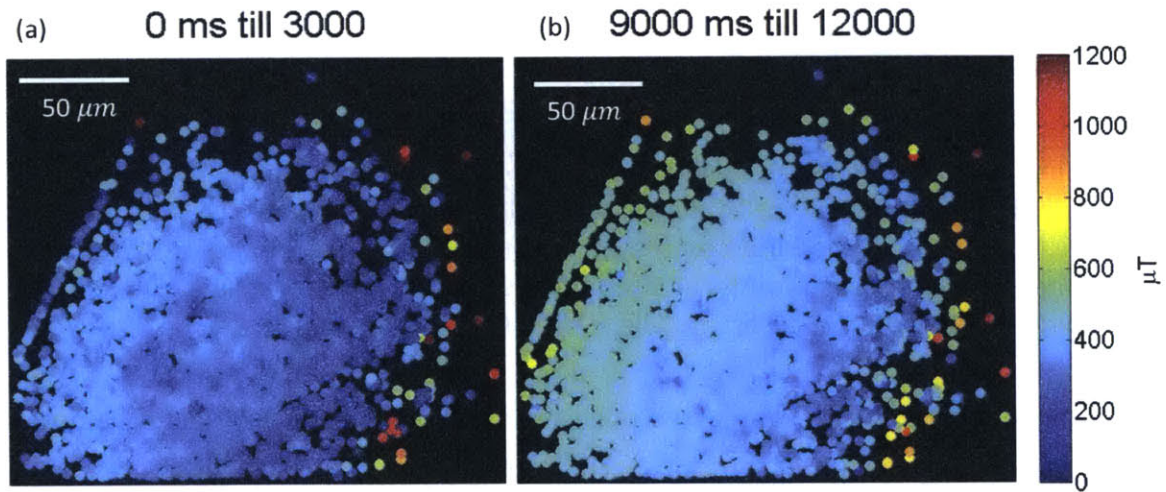


Figure 5-14: **Magnetic field images** Magnetic field images measured through sparse sampling. (a) The interval that this image captures is between 0 to 3 seconds. (b) The interval that this image captures is between 9 to 12 seconds.

image over the first 3 seconds as the current was increased at a rate of 1.4 mA/s (in real time). Fig.5-14b the magnetic image between 9 and 12 seconds.

These results can be summarized in Fig.5-15, where different magnetic images of the increasing DC current in the wire are shown in images Fig.5-15A-C. The total experiment took 70 seconds, real time, to perform. The green dashed lines represent the intervals that the images were averaged over. Image E represents an interpolated magnetic field image at 60mA DC current. This image was generated by fitting each NV's ODMR spectrum. These results confirm that magnetic imaging with nanodia-

Dynamic Magnetic Field Imaging of a Current Carrying Wire

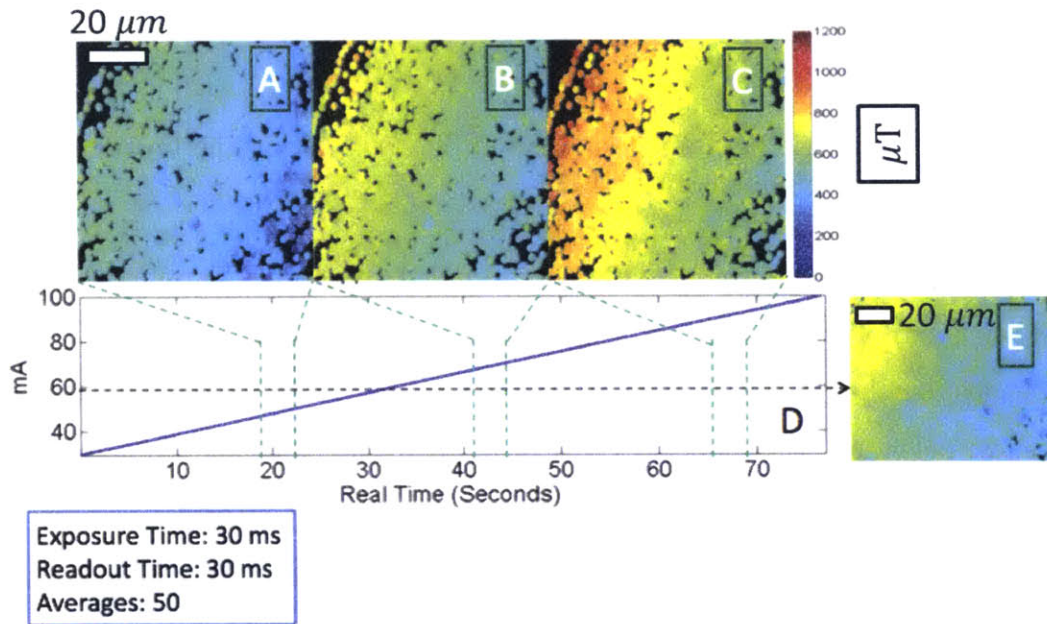


Figure 5-15: Summary of the magnetic field images generated from sparse sampling. A-C show the different magnetic images generated from the increasing DC current in the wire. The green dashed lines represent the intervals that the images were averaged over. Image E represents an interpolated magnetic field image at 60mA DC current. The image was generated by fitting the NV's ODMR spectrum.

monds is possible using an aggregated polycrystalline model and that sparse sampling drastically speeds up the measurement time. The field of view of the measurement was limited by the size of the excitation beam as previously discussed. In this instance the field of view was $10 \mu\text{m} \times 10 \mu\text{m}$ and the associated images were read out at speeds greater than 33 Hz. A total measurement time of 70 seconds, offers the promise of measuring dynamic magnetic phenomenon with NVs in nanodiamonds in living cells.

Chapter 6

Conclusion and Outlook

In this work a spin microscope was constructed to view NVs in nanodiamonds. These nanodiamonds are biologically compatible and can be read out in parallel at high framerates. These NVs were shown to have properties that disagreed with traditional NV systems in bulk diamond with defined crystallographic orientations. A model was presented that treats the NVs within aggregated nanodiamonds as having multiple orientations centered about an origin. This model yields the conclusion that these NV systems can be treated as absolute magnetometers in contrast to NVs within bulk diamond which have been shown to possess magnetic field vector resolution. These results were shown in proof of principle measurement where sparse sampling was used to image the magnetic field of a current carrying wire 101 times faster than curve fitting an ODMR spectrum. These magnetic images were taken over a $100 \mu\text{m}^2$ FOV with associated framerates greater than 33 Hz. These results offer the promise of in vitro measurements of dynamic magnetic phenomenon with NVs in nanodiamonds.

These measurements were done on an electroplated sample that minimized temperature effects of the NV's ODMR curve. Modeling NV's within nanodiamonds as polycrystalline domains was verified by first observing only magnetic effects on the NV's ODMR curves within this magnetic test system. These results were possible because new techniques were developed to electroplate thick gold structures onto number one coverslips through more established fabrication processes such as photolithography and ebeam deposition.

Thermometry and the imaging of thermal profiles was demonstrated in this work. However, a sparse sampling protocol that allows for simultaneous measurements of temperature and magnetic field still needs to be demonstrated. Such a protocol would allow the imaging of temporally and spatially varying magnetic field and temperature at high frame-rates. Such capabilities would be useful in studying electromigration in wires. Electromigration is the process where the critical current density that a metal can maintain is exceeded. In this scenario, wires break down and degrade in a runaway process. Nanodiamonds will be used to image the resulting magnetic fields and thermal profiles during this breakdown to yield insights into how the current behaves as the wire begins to degrade.

The system could be further improved if the sensitivity could be extended by decoupling the laser excitation and MW pulse temporally. The sensitivity could also be enhanced by orders of magnitude by using nanodiamonds with a higher T_2^* time. Further, implanted metallic impurities within the diamond nanocrystals could be used as magnetic amplifiers[55]. These amplifiers would increase the local magnetic field across the nanodiamond. If nanodiamonds could be reliably fabricated that were single crystal and were resilient to aggregation, that would solve many of the limitations of these systems. Various sparse sampling techniques could then be used to perform vectorial magnetic field sensing. Further, super-resolution techniques with high magnetic field gradients could be implemented to improve the spatial resolution of these systems [12].

Bibliography

- [1] *AZ 5214 E Image Reversal Photoresist Product Data Sheet.*
- [2] *E-beam STANDARD OPERATING PROCEDURE.*
- [3] Spin coater.com - laurell technologies.
- [4] V. M. Acosta, E. Bauch, M. P. Ledbetter, A. Waxman, L.-S. Bouchard, and D. Budker. Temperature Dependence of the Nitrogen-Vacancy Magnetic Resonance in Diamond. *Physical Review Letters*, 104(7):070801, February 2010.
- [5] V. M. Acosta, A. Jarmola, E. Bauch, and D. Budker. Optical properties of the nitrogen-vacancy singlet levels in diamond. 82(20):201202.
- [6] Inc Adamas Nanotechnologies. Adamas nanotechnologies, 2016. [Online; accessed 28-January-20156].
- [7] K. Arai, C. Belthangady, H. Zhang, N. Bar-Gill, S. J. DeVience, P. Cappellaro, A. Yacoby, and R. L. Walsworth. Fourier Magnetic Imaging with Nanoscale Resolution and Compressed Sensing Speed-up using Electronic Spins in Diamond. *arXiv:1409.2749 [cond-mat, physics:quant-ph]*, September 2014. arXiv: 1409.2749.
- [8] Gopalakrishnan Balasubramanian, I. Y. Chan, Roman Kolesov, Mohannad Al-Hmoud, Julia Tisler, Chang Shin, Changdong Kim, Aleksander Wojcik, Philip R. Hemmer, Anke Krueger, Tobias Hanke, Alfred Leitenstorfer, Rudolf Bratschitsch, Fedor Jelezko, and Jrg Wrachtrup. Nanoscale imaging magnetometry with diamond spins under ambient conditions. *Nature*, 455(7213):648–651, October 2008.
- [9] Gopalakrishnan Balasubramanian, Philipp Neumann, Daniel Twitchen, Matthew Markham, Roman Kolesov, Norikazu Mizuochi, Junichi Isoya, Jocelyn Achard, Johannes Beck, Julia Tisler, Vincent Jacques, Philip R. Hemmer, Fedor Jelezko, and Jrg Wrachtrup. Ultralong spin coherence time in isotopically engineered diamond. *Nature Materials*, 8(5):383–387, May 2009.
- [10] Peter A. Bandettini. Functional MRI Limitations and Aspirations. *Neural Correlates of Thinking*, 1:15–38, 2008.

- [11] Yi-Ren Chang, Hsu-Yang Lee, Kowa Chen, Chun-Chieh Chang, Dung-Sheng Tsai, Chi-Cheng Fu, Tsong-Shin Lim, Yan-Kai Tzeng, Chia-Yi Fang, Chau-Chung Han, Huan-Cheng Chang, and Wunshain Fann. Mass production and dynamic imaging of fluorescent nanodiamonds. *Nature Nanotechnology*, 3(5):284–288, May 2008.
- [12] Edward H. Chen, Ophir Gaathon, Matthew E. Trusheim, and Dirk Englund. Wide-Field Multispectral Super-Resolution Imaging Using Spin-Dependent Fluorescence in Nanodiamonds. *Nano Letters*, 13(5):2073–2077, May 2013.
- [13] M. Chipaux, A. Tallaire, J. Achard, S. Pezzagna, J. Meijer, V. Jacques, J.-F. Roch, and T. Debuisschert. Magnetic imaging with an ensemble of Nitrogen Vacancy centers in diamond. *arXiv:1410.0178 [cond-mat]*, October 2014. arXiv: 1410.0178.
- [14] Hannah Clevenson, Matthew E. Trusheim, Tim Schroder, Carson Teale, Danielle Braje, and Dirk Englund. Broadband Magnetometry and Temperature Sensing with a Light Trapping Diamond Waveguide. *arXiv:1406.5235 [cond-mat, physics:physics, physics:quant-ph]*, June 2014. arXiv: 1406.5235.
- [15] Peter Dek, Blint Aradi, Moloud Kaviani, Thomas Frauenheim, and Adam Gali. Formation of NV centers in diamond: A theoretical study based on calculated transitions and migration of nitrogen and vacancy related defects. *Physical Review B*, 89(7):075203, February 2014.
- [16] Stephen J. DeVience, Linh M. Pham, Igor Lovchinsky, Alexander O. Sushkov, Nir Bar-Gill, Chinmay Belthangady, Francesco Casola, Madeleine Corbett, Huiliang Zhang, Mikhail Lukin, Hongkun Park, Amir Yacoby, and Ronald L. Walsworth. Nanoscale NMR spectroscopy and imaging of multiple nuclear species. *Nature Nanotechnology*, 10(2):129–134, February 2015.
- [17] M. W. Doherty, V. M. Acosta, A. Jarmola, M. S. J. Barson, N. B. Manson, D. Budker, and L. C. L. Hollenberg. Temperature shifts of the resonances of the NV center in diamond. *Physical Review B*, 90(4):041201, July 2014.
- [18] M. W. Doherty, F. Dolde, H. Fedder, F. Jelezko, J. Wrachtrup, N. B. Manson, and L. C. L. Hollenberg. Theory of the ground-state spin of the NV⁻ center in diamond. *Physical Review B*, 85(20):205203, May 2012.
- [19] F. Dolde, H. Fedder, M. W. Doherty, T. Nbauer, F. Rempp, G. Balasubramanian, T. Wolf, F. Reinhard, L. C. L. Hollenberg, F. Jelezko, and J. Wrachtrup. Electric-field sensing using single diamond spins. *Nature Physics*, 7(6):459–463, June 2011.
- [20] A. Drau, M. Lesik, L. Rondin, P. Spinicelli, O. Arcizet, J.-F. Roch, and V. Jacques. Avoiding power broadening in optically detected magnetic resonance of single NV defects for enhanced DC-magnetic field sensitivity. *arXiv:1108.0178 [cond-mat]*, July 2011. *Phys. Rev. B* 84, 195204 (2011).

- [21] Chi-Cheng Fu, Hsu-Yang Lee, Kowa Chen, Tsong-Shin Lim, Hsiao-Yun Wu, Po-Keng Lin, Pei-Kuen Wei, Pei-Hsi Tsao, Huan-Cheng Chang, and Wunshain Fann. Characterization and application of single fluorescent nanodiamonds as cellular biomarkers. *Proceedings of the National Academy of Sciences*, 104(3):727–732, January 2007.
- [22] Michael Geiselmann, Mathieu L. Juan, Jan Renger, Jana M. Say, Louise J. Brown, F. Javier Garca de Abajo, Frank Koppens, and Romain Quidant. Three-dimensional optical manipulation of a single electron spin. 8(3):175–179.
- [23] Michael Gould, Russell J. Barbour, Nicole Thomas, Hamed Arami, Kannan M. Krishnan, and Kai-Mei C. Fu. Room-temperature detection of a single 19 nm super-paramagnetic nanoparticle with an imaging magnetometer. *Applied Physics Letters*, 105(7):072406, August 2014.
- [24] L. T. Hall, G. C. G. Beart, E. A. Thomas, D. A. Simpson, L. P. McGuinness, J. H. Cole, J. H. Manton, R. E. Scholten, F. Jelezko, Jrg Wrachtrup, S. Petrou, and L. C. L. Hollenberg. High spatial and temporal resolution wide-field imaging of neuron activity using quantum NV-diamond. *Scientific Reports*, 2, May 2012.
- [25] G.E. Harlow. *The Nature of Diamonds*.
- [26] Moritz V. Hauf, Patrick Simon, Nabeel Aslam, Matthias Pfender, Philipp Neumann, Sbastien Pezzagna, Jan Meijer, Jrg Wrachtrup, Martin Stutzmann, Friedemann Reinhard, and Jos A. Garrido. Addressing Single Nitrogen-Vacancy Centers in Diamond with Transparent in-Plane Gate Structures. *Nano Letters*, 14(5):2359–2364, May 2014.
- [27] Eugene Hecht. *Optics, 2nd Edition*.
- [28] Philip Hemmer. Toward Molecular-Scale MRI. *Science*, 339(6119):529–530, February 2013.
- [29] Irena Kratochvilova, Jakub Sebera, Petr Ashcheulov, Martin Golan, Miroslav Ledvina, Julia Micova, Filip Mravec, Alexander Kovalenko, Dmitry Zverev, Boris V. Yavkin, Sergei B. Orlinskii, Stanislav Zalis, Anna Fiserova, Jan Richter, Ludek Sefc, and Jaroslav Turnek. Magnetical and Optical Properties of Nanodiamonds Can Be Tuned by Particles Surface Chemistry: Theoretical and Experimental Study. *The Journal of Physical Chemistry C*, September 2014.
- [30] G. Kucsko, P. C. Maurer, N. Y. Yao, M. Kubo, H. J. Noh, P. K. Lo, H. Park, and M. D. Lukin. Nanometre-scale thermometry in a living cell. *Nature*, 500(7460):54–58, August 2013.
- [31] Christian Kurtsiefer, Sonja Mayer, Patrick Zarda, and Harald Weinfurter. Stable Solid-State Source of Single Photons. *Physical Review Letters*, 85(2):290–293, July 2000.

- [32] D. Le Sage, K. Arai, D. R. Glenn, S. J. DeVience, L. M. Pham, L. Rahn-Lee, M. D. Lukin, A. Yacoby, A. Komeili, and R. L. Walsworth. Optical magnetic imaging of living cells. *Nature*, 496(7446):486–489, April 2013.
- [33] Kangmook Lim, Chad Ropp, Benjamin Shapiro, Jacob M. Taylor, and Edo Waks. Scanning localized magnetic fields in a microfluidic device using single spin in a nano-diamond. *arXiv:1407.1452 [cond-mat, physics:physics, physics:quant-ph]*, July 2014. arXiv: 1407.1452.
- [34] Lipson Lipson and Tannhauser. *Optical Physics*.
- [35] B. J. Maertz, A. P. Wijnheijmer, G. D. Fuchs, M. E. Nowakowski, and D. D. Awschalom. Vector magnetic field microscopy using nitrogen vacancy centers in diamond. *Applied Physics Letters*, 96(9):092504, March 2010.
- [36] J. R. Maze, P. L. Stanwix, J. S. Hodges, S. Hong, J. M. Taylor, P. Cappellaro, L. Jiang, M. V. Gurudev Dutt, E. Togan, A. S. Zibrov, A. Yacoby, R. L. Walsworth, and M. D. Lukin. Nanoscale magnetic sensing with an individual electronic spin in diamond. *Nature*, 455(7213):644–647, October 2008.
- [37] L. P. McGuinness, Y. Yan, A. Stacey, D. A. Simpson, L. T. Hall, D. Maclaurin, S. Praver, P. Mulvaney, J. Wrachtrup, F. Caruso, R. E. Scholten, and L. C. L. Hollenberg. Quantum measurement and orientation tracking of fluorescent nanodiamonds inside living cells. *Nature Nanotechnology*, 6(6):358–363, June 2011.
- [38] P. Neumann, I. Jakobi, F. Dolde, C. Burk, R. Reuter, G. Waldherr, J. Honert, T. Wolf, A. Brunner, J. H. Shim, D. Suter, H. Sumiya, J. Isoya, and J. Wrachtrup. High-Precision Nanoscale Temperature Sensing Using Single Defects in Diamond. *Nano Letters*, 13(6):2738–2742, June 2013.
- [39] B. K. Ofori-Okai, S. Pezzagna, K. Chang, M. Loretz, R. Schirhagl, Y. Tao, B. A. Moores, K. Groot-Berning, J. Meijer, and C. L. Degen. Spin properties of very shallow nitrogen vacancy defects in diamond. *Physical Review B*, 86(8):081406, August 2012.
- [40] I. I. Rabi, J. R. Zacharias, S. Millman, and P. Kusch. A New Method of Measuring Nuclear Magnetic Moment. *Physical Review*, 53(4):318–318, February 1938.
- [41] J. Y. Raty and G. Galli. Optical properties and structure of nanodiamonds. *Journal of Electroanalytical Chemistry*, 584(1):9–12, October 2005.
- [42] L. Rondin, J.-P. Tetienne, T. Hingant, J.-F. Roch, P. Maletinsky, and V. Jacques. Magnetometry with nitrogen-vacancy defects in diamond. *arXiv:1311.5214 [cond-mat]*, November 2013.
- [43] L. Rondin, J.-P. Tetienne, S. Rohart, A. Thiaville, T. Hingant, P. Spinicelli, J.-F. Roch, and V. Jacques. Stray-field imaging of magnetic vortices with a single diamond spin. *Nature Communications*, 4, July 2013.

- [44] Susanta K. Sarkar, Ambika Bumb, Xufeng Wu, Kem A. Sochacki, Peter Kellman, Martin W. Brechbiel, and Keir C. Neuman. Wide-field in vivo background free imaging by selective magnetic modulation of nanodiamond fluorescence. *Biomedical Optics Express*, 5(4):1190–1202, April 2014.
- [45] James H. Scatliff and Peter J. Morris. From Roentgen to magnetic resonance imaging: the history of medical imaging. *North Carolina Medical Journal*, 75(2):111–113, April 2014.
- [46] Eike Schfer-Nolte, Lukas Schlipf, Markus Ternes, Friedemann Reinhard, Klaus Kern, and Jrg Wrachtrup. Tracking Temperature Dependent Relaxation Times of Individual Ferritin Nanomagnets with a Wide-band Quantum Spectrometer. *Physical Review Letters*, 113(21), November 2014. arXiv: 1406.0362.
- [47] Romana Schirhagl, Kevin Chang, Michael Loretz, and Christian L. Degen. Nitrogen-Vacancy Centers in Diamond: Nanoscale Sensors for Physics and Biology. *Annual Review of Physical Chemistry*, 65(1):83–105, 2014.
- [48] Rolf Simon Schoenfeld and Wolfgang Harneit. Real Time Magnetic Field Sensing and Imaging Using a Single Spin in Diamond. *Physical Review Letters*, 106(3):030802, January 2011.
- [49] W. Schottky. ber spontane Stromschwankungen in verschiedenen Elektrizittsleitern. *Annalen der Physik*, 362(23):541–567, January 1918.
- [50] B. D. Schrag, Xiaoyong Liu, Weifeng Shen, and Gang Xiao. Current density mapping and pinhole imaging in magnetic tunnel junctions via scanning magnetic microscopy. *Applied Physics Letters*, 84(15):2937–2939, April 2004.
- [51] S. Steinert, F. Dolde, P. Neumann, A. Aird, B. Naydenov, G. Balasubramanian, F. Jelezko, and J. Wrachtrup. High sensitivity magnetic imaging using an array of spins in diamond. *Review of Scientific Instruments*, 81(4):043705, April 2010.
- [52] S. Steinert, F. Ziem, L. T. Hall, A. Zappe, M. Schweikert, N. Gtz, A. Aird, G. Balasubramanian, L. Hollenberg, and J. Wrachtrup. Magnetic spin imaging under ambient conditions with sub-cellular resolution. *Nature Communications*, 4:1607, March 2013.
- [53] J. M. Taylor, P. Cappellaro, L. Childress, L. Jiang, D. Budker, P. R. Hemmer, A. Yacoby, R. Walsworth, and M. D. Lukin. High-sensitivity diamond magnetometer with nanoscale resolution. *Nature Physics*, 4(10):810–816, October 2008.
- [54] J.-P. Tetienne, T. Hingant, L. J. Martinez, S. Rohart, A. Thiaville, L. Herrera Diez, K. Garcia, J.-P. Adam, J.-V. Kim, J.-F. Roch, I. M. Miron, G. Gaudin, L. Vila, B. Ocker, D. Ravelosona, and V. Jacques. The nature of domain walls in ultrathin ferromagnets revealed by scanning nanomagnetometry. *arXiv:1410.1313 [cond-mat]*, October 2014. arXiv: 1410.1313.

- [55] Luka Trifunovic, Fabio L. Pedrocchi, Silas Hoffman, Patrick Maletinsky, Amir Yacoby, and Daniel Loss. High-efficiency resonant amplification of weak magnetic fields for single spin magnetometry at room temperature. *Nature Nanotechnology*, advance online publication, May 2015.
- [56] Wikipedia. Ampere's circuital law — wikipedia, the free encyclopedia, 2015. [Online; accessed 27-August-2015].
- [57] Wikipedia. Diamond — wikipedia, the free encyclopedia, 2015. [Online; accessed 22-August-2015].
- [58] Wikipedia. Diamond cubic — wikipedia, the free encyclopedia, 2015. [Online; accessed 22-August-2015].
- [59] Wikipedia. Electron beam physical vapor deposition — wikipedia, the free encyclopedia, 2015. [Online; accessed 23-August-2015].
- [60] Wikipedia. Electroplating — wikipedia, the free encyclopedia, 2015. [Online; accessed 23-August-2015].
- [61] Wikipedia. Functional magnetic resonance imaging — wikipedia, the free encyclopedia, 2015. [Online; accessed 24-August-2015].
- [62] Wikipedia. Geometrical optics — wikipedia, the free encyclopedia, 2015. [Online; accessed 27-August-2015].
- [63] Kirt R. Williams, Senior Member, Kishan Gupta, Student Member, and Matthew Wasilik. *Etch Rates for Micromachining Processing Part II*.